

## Role of viscous plate coupling in the late Tertiary Andean tectonics

Gonzalo Yáñez

Corporación Nacional del Cobre, Chile, Santiago, Chile

José Cembrano

Departamento de Ciencias Geológicas, Universidad Católica del Norte, Antofagasta, Chile

Received 13 March 2003; revised 21 November 2003; accepted 9 December 2003; published 18 February 2004.

[1] Plate coupling between oceanic and continental plates in convergent margins of Andean type is analyzed from the continuum mechanics approach. We postulate a simple mechanism that accounts for the compressive regime in Andean-type environments. In this mechanism, deformation in the continental lithosphere is split into two distinctive domains: The forearc domain and the arc-foreland domain. The forearc deformation is controlled by the balance between buoyancy forces associated with the trench and continental slope relief and the stress transferred from the convergence velocity through the age- and velocity-dependent slip zone. The arc-foreland deformation is controlled by the absolute plate velocity of the continental plate and the resistance at the slip zone. Strength of the coupling zone is determined by analyzing the dynamic trench topography along the active margin of South America between 0 and 55°S. Using this approach, we found strength values in the range of 20–95 MPa, in strong direct correlation with the age of the subducting plate. The slip layer strength observation has been successfully tested against a thermal- and strain rate-dependent rheological model. From this theoretical result we define an empirical relationship between strength of the slip zone and the age and convergence velocity. Applying this plate coupling model, we reproduce shortening rates in the order of 1–10 km/Myr, in agreement with those reported for the late Tertiary evolution of the Andes. Model results reproduce some first-order features of the geological evolution of the margin, such as the shape of the trench, the overall Andes relief, the Altiplano buildup, and block rotation patterns. In addition, the model provides a mechanism to explain the evolution of the Central Depression, the inversion of Tertiary basins under slow convergence rates during the Miocene, and the segmentation of the margins tectonic erosion. **INDEX TERMS:** 8120 Tectonophysics: Dynamics of lithosphere and mantle—general; 8149 Tectonophysics: Planetary tectonics (5475); 8150 Tectonophysics: Plate boundary—general (3040); 8159 Tectonophysics: Rheology—crust and lithosphere; 8164 Tectonophysics: Stresses—crust and lithosphere; **KEYWORDS:** Andean, tectonics, viscous plate coupling

**Citation:** Yáñez, G., and J. Cembrano (2004), Role of viscous plate coupling in the late Tertiary Andean tectonics, *J. Geophys. Res.*, 109, B02407, doi:10.1029/2003JB002494.

### 1. Introduction

[2] Distributed deformation along noncollisional orogens has traditionally been attributed to oceanic plate subduction underneath the much weaker continental lithosphere [Dewey and Bird, 1970]. The Andes, in particular (Figure 1), has been regarded as the classical-type example of this kind of plate interaction because of the high degree of coupling between oceanic and continental plates [Uyeda and Kanomari, 1979]. Such a strong coupling has been genetically associated with a high convergence rate and relatively young and buoyant oceanic plate [e.g., Jarrard, 1986]. Although the Andean-type compressive regime is clearly different from the Mariana-type extensional regime

as a result of controlling factors such as convergence rate and age of the subducting plate [Uyeda and Kanomari, 1979], such a simple mechanism alone cannot account for the marked along strike differences in the late Tertiary tectonic evolution of the central and southern Andes (10–40°S). Thus, in contrast with common beliefs based upon this simple model, the greatest late Tertiary deformation occurs in the Altiplano region of the central Andes [e.g., Lamb and Hoke, 1997] in close spatial association with the oldest subducting plate of the margin (40–50 Ma). Total estimated shortening amounts for the Altiplano-Eastern Cordillera-Subandean zone from ~40 Ma are in the range of 250–300 km [e.g., McQuarrie, 2002a; Muller et al., 2002]. In contrast, the southern central Andes (south of 30°S) shows evidence of much smaller shortening amounts (less than ~100 km) during the same time span [e.g., Ramos, 1985; Allmendinger et al., 1990; Jordan et al.,

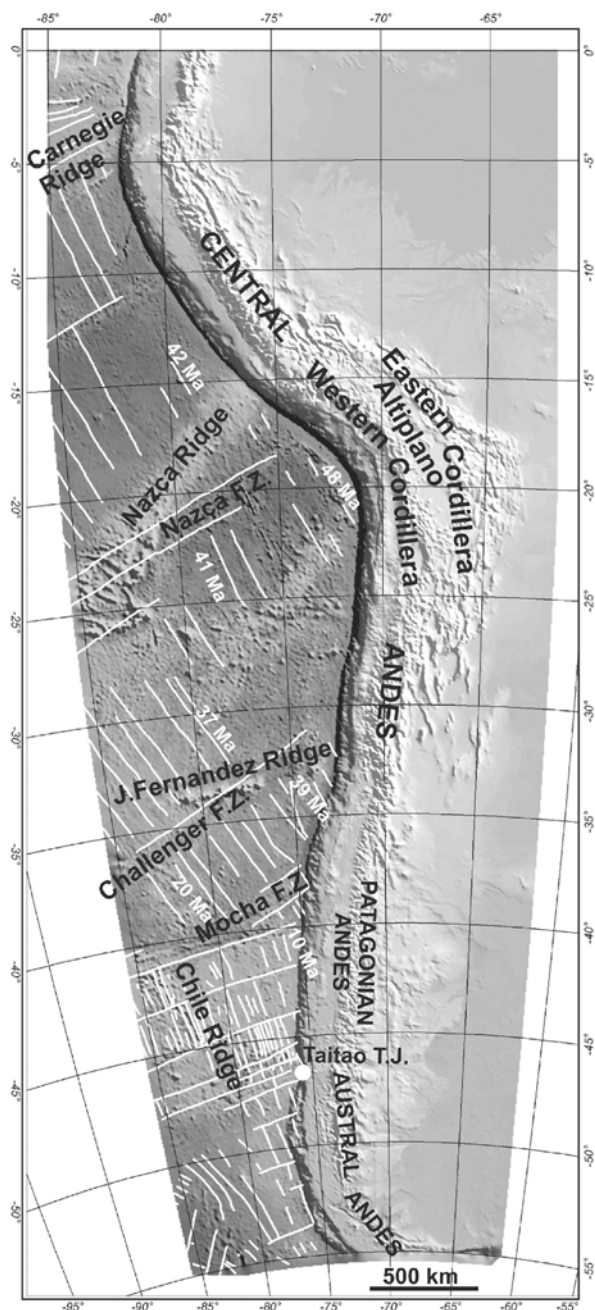


**Figure 1.** Location map of South American active margin and main offshore and onshore tectonic features as discussed in the text. Note the age of subducting Nazca Plate in white.

2001], in close spatial association with a significantly younger oceanic plate, toward the triple junction at the Taitao Peninsula (47°S). Considering the Andean orogenesis as the result of crustal shortening through folding and faulting under a roughly common convergence regime [e.g., Jordan *et al.*, 1983; Ramos, 1989], the observed along-strike variations must be linked to either rheological heterogeneities within the continental plate and/or different degrees of stress transference from the oceanic to the overriding plate. For instance, previous authors have relied

upon the intrinsic properties of the continental lithosphere to explain the origin of the Altiplano plateau [e.g., Lamb and Hoke, 1997; Isacks, 1988], or inherited conditions from previous evolutions of the margin as a whole [e.g., Jordan *et al.*, 2001]. The role of interplate coupling through episodic subduction of flat slab segments, has been largely emphasized [e.g., Jordan *et al.*, 1983; Gutscher, 2002]. However, seismicity at the interplate contact is essentially equivalent to nonflat slab segments [see, e.g., Gutscher, 2002]. The larger seismic moment release of flat slab segments is associated with intraplate seismicity, due to the presence of a cool slab in the flat segment. Thus the overriding plate total amount of shortening through time is not necessarily incremented within flat slab segments.

[3] In order to assess the role of intraplate coupling in the Andes, we develop a simplified 2.5-dimensional (2.5-D) deformation model using the thin viscous sheet approximation [England and McKenzie, 1982], with a localized traction along the Benioff plane (section 2). In this model the localized traction represents the weak interplate zone or slip layer [e.g., Jischke, 1975; Wdowinski, 1992; Daniel *et al.*, 2001]. Using the relationship between the slip layer and the dynamic trench topography [Wdowinski, 1992], in section 3 we address the along-strike variations of the slip layer parameter in the Andes. This was achieved by determining the appropriate plate coupling that equilibrates tectonic and buoyancy forces at the trench. In section 4 we study the rheology of the slip zone considering its thermal (age) and strain rate (convergence velocity) dependence, postulating an empirical relationship for the strength of the coupling zone. This empirical relationship for the plate coupling, is incorporated into the proposed 2.5-D deformation model, and used later on to study the late Tertiary (25–0 Ma) evolution of the Andean margin (section 5). We focused the analysis on this time period because kinematics of convergence is well constrained [e.g., Tebbens and Cande, 1997].

## 2. Plate Interaction at Andean-Type Subduction Zones

[4] One fundamental constraint for the orogenic processes in the Andes is that the active margin of South America was basically under noncompressive to extensional regime prior to the opening of the south Atlantic (Late Jurassic to Early Cretaceous) [e.g., Mpodozis and Ramos, 1990; Aberg *et al.*, 1984]. However, magmatic products associated with subduction were widely distributed along the margin since the Triassic [e.g., Parada *et al.*, 1991]. Thus subduction by itself cannot account for the so-called “Andean-type orogenesis” in which the mountain building process is largely controlled by shortening of the crust through folding and faulting, that is driven by oceanic continental plate convergence [e.g., Jordan *et al.*, 2001]. In addition, the geological record indicates that the margin tectonics is clearly segmented along strike. Furthermore, from the Altiplano region northward and southward, there is a marked decrease in the total amount of shortening, without an obvious direct correspondence with either the slab age [Jordan *et al.*, 1983; McQuarrie, 2002a], or convergence rates [Jordan *et al.*, 2001]. One way to confront and reconcile geological observations with plate tectonics is to incorporate oceanic

crust age heterogeneity in large-scale deformation models. Oceanic plate age heterogeneity is quite common in convergent margins, and is caused by different factors such as oblique convergence, fracture zones with large age offset, and collision of active or passive ridges.

## 2.1. Conceptual Model

[5] The proposed model incorporates two complementary approaches: The thin viscous sheet approximation (originally developed by *England and McKenzie* [1982] and also by *Bird* [1988]) and the slip layer concept developed by *Wdowinski* [1992]. The thin viscous sheet approximation has been used to reduce 3-D deformation problems into 2.5-D, assuming plane strain deformation and integrating rheological and density heterogeneity with depth. In the original formulation of *England and McKenzie* [1982], shear traction at the base of the lithosphere was neglected, assuming an inviscid asthenosphere coupling. However, in subduction environment, traction at the plate coupling zone cannot be neglected. In fact, we postulate that interplate coupling actually drives the overriding plate deformation. On the other hand, the plate coupling behavior can be studied using the slip layer concept [*Wdowinski*, 1992] and its relationship with the dynamic trench topography. According to *Wdowinski* [1992] and further extended by *Wdowinski and Bock* [1994], the trench topography is the result of a dynamic balanced between tectonic and buoyancy forces. In this approach, the slip layer strength represents the degree of plate coupling that deforms the forearc (and, in particular, the trench region) to equilibrate tectonic forces. As we will show in section 3, using present-day tectonics and trench topography in the Andes, we can estimate the strength of the slip layer and derive an empirical relationship that allows its incorporation as shear traction in the 2.5-D deformation model. One important conclusion of *Wdowinski* [1992] is that after a transient period (1–10 Ma), the dynamic trench topography absorbs almost all the deformation associated with the subduction process. On the basis of this observation we postulate that the continental-scale deformation problem in Andean-type convergence zones can be separated into two large tectonic domains: (1) a forearc domain, in which the dynamic trench topography is basically controlled by the difference between the oceanic and forearc plate velocities ( $U_{NA}-U_{FA}$ : Modified convergence velocity), and the slip layer strength, and (2) an intra-arc-foreland domain, in which deformation is controlled by intrinsic rheological properties of the medium, the strength of the slip layer and the absolute velocity of the continental plate. A schematic cartoon of the proposed model is shown in Figure 2a.

[6] According to this model, deformation of the forearc region can be modified by changes in the modified convergence velocity and by the age of oceanic crust being subducted. Their effects on the foreland region would be only transient phenomena while equilibrium of the dynamic trench topography is reached. *Wdowinski* [1992] suggests that equilibrium is reached in 5–10 Myr for a new subduction zone; therefore changes in already formed subduction zones would reach equilibrium in a fraction of this time. In contrast, deformation in the intra-arc and foreland regions is

controlled by the absolute velocity of the continental plate ( $U_{SA}$ ) and the traction at the slip layer that resists thrusting of the continental plate over a static oceanic plate. Normally, traction at the slip layer is not capable to resist the whole plate motion, and therefore there is an absolute forearc velocity ( $U_{FA}$ ) in the trenchward direction. The difference between the continental plate velocity and the forearc velocity is the shortening absorbed in the deforming arc and foreland zone. One interesting characteristic of this model is that given the fact that  $U_{SA}$  is essentially the same for the whole margin, deformation in the arc and foreland region is basically controlled by the traction at the slip layer. As we will show in section 3, traction at the slip layer is not only a function of the convergence velocity but most important the age of the oceanic crust at the trench, providing in this way a transient dependence beyond the plate tectonic fate. In addition, isolating the tectonic control of the continental deformation in the  $U_{SA}$  component of the convergence, we can also explain the already mentioned observation of noncompressive regime prior to the opening of the South Atlantic.

[7] One difficulty arising from the previous conceptual model is that forearc velocity ( $U_{FA}$ ) cannot be determined a priori. However, given the fact that  $U_{FA}$  would be a fraction of the continental plate velocity, which is  $\sim 20\%$  of the oceanic plate velocity, its influence in the slip layer resistance is probably  $<10\%$  and with minor differences along strike. Therefore, as a first approximation, we neglect its effect in the modified convergence velocity for the purpose of estimating the slip layer viscosity.

## 2.2. Viscous Domains

[8] The central role of power law mechanisms of continental lithosphere deformation has been largely recognized in continuum approaches [e.g., *England and McKenzie*, 1982; *England*, 1983; *Bird and Piper*, 1980]. Deformation in this strain-dependent rheology allows a better fit for high strain rate regions. In order to keep our model as simple as possible but retaining the essentials of the position-dependent rheology, we define four viscous domains as (1) slip zone, (2) forearc, (3) arc-foreland, and (4) cratonic, with distinctive but constant (Newtonian) rheological properties.

[9] The slip zone represents the coupling between the oceanic and the continental plate. Its power law rheology and thermal (oceanic plate age) dependence will be covered in section 4; however, for a given convergence segment its value is basically constant. In terms of effective viscosity this domain represents the weakest part of the deforming system, with values in the range of  $10^{19}$  to  $5 \cdot 10^{20}$  Pa s, for an arbitrary slip layer thickness of 10 km. Similar numbers have been used in the literature to characterize the slip layer [e.g., *Wdowinski and Bock*, 1994; *Daniel et al.*, 2001].

[10] In the postulated conceptual model the forearc deformation balances the tectonic and buoyancy forces through the dynamic trench topography. If this equilibrium is reached in timescales shorter than 5–10 Myr (a critical, and poorly constrained, condition that depends on the rheology of the forearc region itself), the rheology of this domain is dominated by a low strain rate asymptotic behavior [e.g., *Ranalli*, 1995]. In fact, following *Christensen's* [1992] formulation, effective viscosity ( $\eta_{eff}$ ) can be expressed in terms of two competing effects: A strain rate-



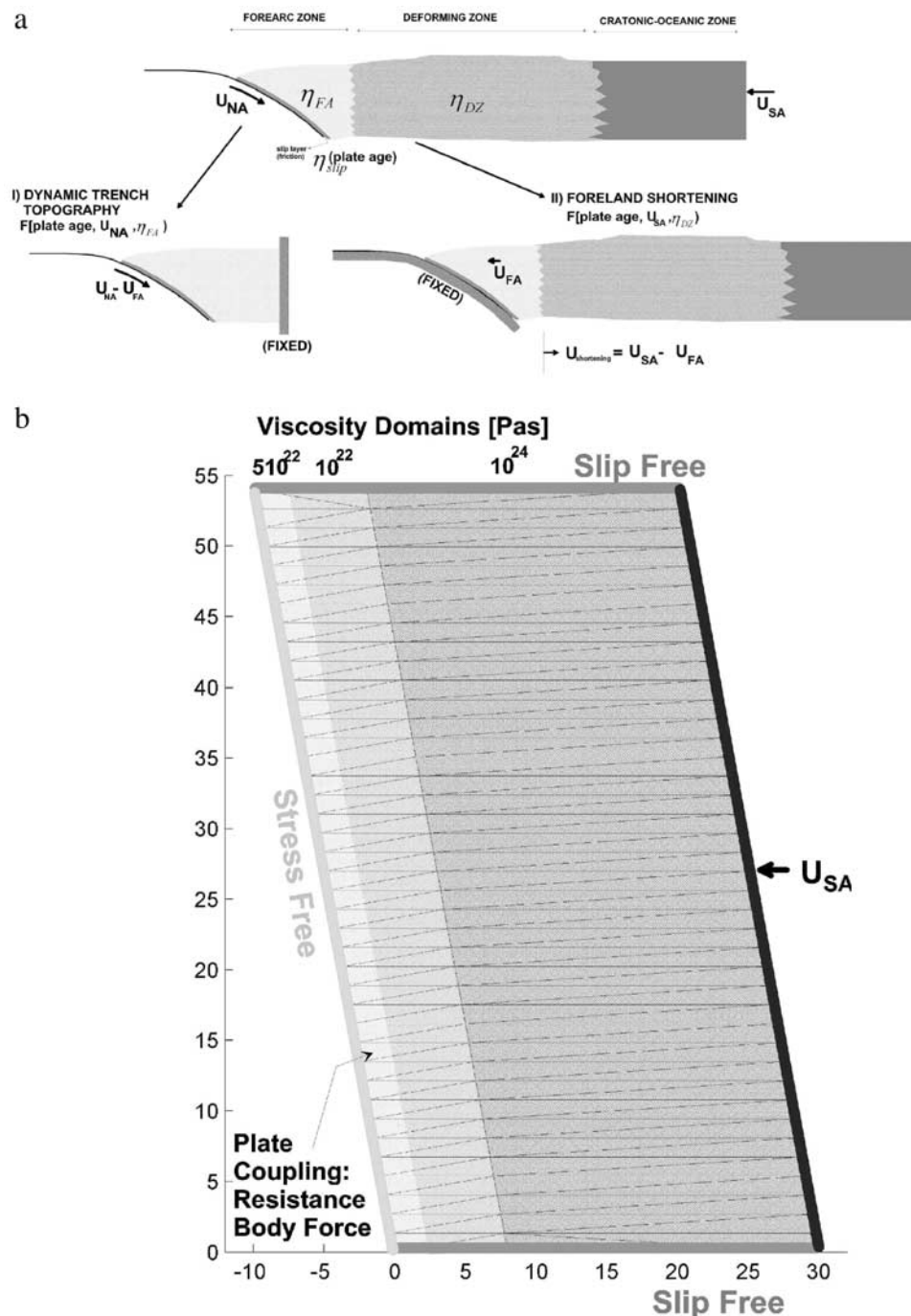


**Figure 2.** (a) Cartoon representation of the boundary conditions for the proposed model. (top) Overall representation of the problem. Tectonic forces are expressed in terms of the absolute plate velocities of the oceanic ( $\mathbf{U}_{\text{Nazca}}$ ) and continental plate ( $\mathbf{U}_{\text{SA}}$ ). The three tectonic domains are shown (forearc, deforming zone, and cratonic-oceanic) and the slip layer zone at the interplate contact. (bottom) Problem splits into two zones. (left) Forearc zone, in which the deformation is controlled by the velocity of the oceanic plate, the slip layer, and forearc viscosities. (right) Bulk deformation in the arc and foreland zone controlled by the “ridge push”-driven continental velocity, the rheology of the deforming zone, and the resistance at the slip layer. In this arc-foreland zone the oceanic plate is kept fixed, as the continental plate overthrusts it at a rate which is a function of the resistance at the slip layer zone. (b) Mesh definition, boundary conditions, and material properties for a generalized arc-foreland-deforming zone. Horizontal and vertical dimensions correspond to units of 100 km; thus the mesh has a dimension of roughly 5400 by 3000 km. Viscosities of the three domains defined in the text represent the forearc ( $5 \times 10^{22}$  Pa s), deforming zone ( $5 \times 10^{22}$  Pa s), and cratonic-oceanic ( $10^{24}$  Pa s), respectively. The applied boundary conditions are indicated on the edges of the mesh domain. Also included is the age-dependent resistance body force in the interplate contact with the oceanic plate.

dependent nonlinear component ( $\eta_{nl}$ ) and a constant component ( $\eta_o$ ):

$$\eta = \left[ \frac{1}{\eta_{nl}} + \frac{1}{\eta_o} \right]^{-1}.$$

At high strain rates the power law rheology conditions a reduction in the nonlinear viscosity, thus dominating the effective viscosity. In contrast, under low strain rates, such as the equilibrium condition in the dynamic trench topography of the forearc domain, the nonlinear viscosity becomes larger than the constant component; therefore the effective viscosity is dominated by the constant component. Following literature estimates [e.g., *Wdowski and Bock*, 1994; *Daniel et al.*, 2001], we adopt a forearc viscosity of  $5 \times 10^{22}$  Pa s that allows a dynamic trench equilibrium in less than 5–10 Myr [*Wdowski*, 1992].

[11] In the arc-foreland and cratonic domains the strongest mantle lithosphere and the associated thermal field control the power law rheology [e.g., *England and McKenzie*, 1982]. According to *England* [1983] the strength of the continental lithosphere can be approximated by  $\approx (B\dot{\epsilon}^{1/n} T_M^2 nR/Q\gamma) \exp(Q/nRT_M)$ , where  $B$ ,  $n$ , and  $Q$  are rheological parameters,  $R$  is the universal gas constant ( $8.31 \text{ J mol}^{-1} \text{ } ^\circ\text{K}^{-1}$ ),  $\dot{\epsilon}$  is the strain rate,  $\gamma$  is the thermal gradient, and  $T_M$  is the absolute temperature at the Moho. Dividing this expression by 2 times the strain rate and the lithospheric thickness ( $L$ ), we obtain an approximate estimate of the effective viscosity in the lithosphere:

$$\eta_{\text{eff}} \approx \frac{B\dot{\epsilon}^{1-1/n} T_M^2 nR}{2Q\gamma L} \exp\left(\frac{Q}{nRT_M}\right).$$

Using the rheology of the olivine to characterize the strongest layer in the lithosphere [e.g., *England and McKenzie*, 1982; *England*, 1983; *Bird and Piper*, 1980],  $B$ ,  $n$ , and  $Q$ , become  $7.9 \text{ Pa s}^{1/3}$ , 4, and  $500 \text{ kJ mol}^{-1}$ , respectively. Average thermal gradients for the arc and cratonic regions are  $\sim 16$  and  $\sim 10^\circ\text{C/km}$ , respectively, which means a temperature at the Moho (40–60 km deep in the arc and 35 km in cratonic regions) of  $600$ – $700^\circ\text{C}$  and  $450^\circ\text{C}$ , respectively. From geological estimates [e.g., *Isacks*, 1988; *Lamb and Hoke*, 1997] the strain rate is probably in the range of  $10^{-13}$  to  $10^{-15} \text{ s}^{-1}$ . Evaluating the previous expression with  $T_M = 600^\circ\text{C}$  and a strain rate of  $10^{-14} \text{ s}^{-1}$ , as the characteristic parameters in the arc-foreland domain, we obtain an effective viscosity of  $10^{22} \text{ Pa s}$ . The critical parameter in this estimate is the Moho depth, which evolves from about 35 to 55 km during orogenesis, with a progressive reduction in the effective viscosity. The adopted reference viscosity of  $10^{22} \text{ Pa s}$  overestimates the real values at the initial stages of crustal thickening, but later on, real values are underestimated, such that the net result is about right if we are not concerned with local-scale deformation processes. In the cratonic zone, strain rate, the thermal gradient, and the temperature at the Moho condition an effective viscosity which is at least 2–3 orders of magnitude higher than the appropriate numbers for the arc-foreland domain. In the following computations we adopt a rather conservative reference number of  $10^{24} \text{ Pa s}$ , which means that

deformation is basically accommodated in the arc-foreland region, with a virtually rigid cratonic area.

### 2.3. The 2.5-D Thin Viscous Formulation for Subducting Margins

[12] Applying the conceptual model described above, we now formulate a theoretical adaptation of the thin viscous sheet approach in terms of the slip layer strength. The thin viscous approximation of *England and McKenzie* [1982] reduces the 3-D problem into a horizontal domain by integration of the vertical component and takes into account the body forces associated with crustal thickness (2.5-D). Kinematic and/or dynamic boundary conditions are then applied at the boundaries. Although the general formulation of *England and McKenzie* [1982] considers a power law rheology, the Newtonian approach used in this case keeps the basics of a position-dependent rheology under the definition of distinctive viscous domains (section 2.2). The traction at the base of the lithosphere is neglected in the formulation of *England and McKenzie* [1982]. However, in subduction environments it represents the interplate coupling, which is limited by the inclined Benioff plane; therefore  $L$  is a function of the position  $L(x)$ . Following *England and McKenzie* [1982] approach, but considering the traction at the base Benioff plane, the thin viscous problem can be written in the following compact form:

$$\frac{\partial}{\partial x_i} \left[ \eta \left( 2 \frac{\partial u_i}{\partial x_i} + \frac{\partial u_j}{\partial x_j} \right) \right] + \frac{\partial}{\partial x_j} \left[ \eta \left( \frac{\partial u_i}{\partial x_j} + \frac{\partial u_j}{\partial x_i} \right) \right] = ArS \frac{\partial S}{\partial x_i} - \frac{L_o^2}{\eta_o} \frac{\tau_{iz}}{L(x)},$$

where index  $i, j$  represents the  $x$  or  $y$  component (when  $i = x$  then  $j = y$ , and vice versa),  $u_i$  is horizontal velocity,  $\eta$  is effective viscosity,  $g$  is gravity acceleration,  $L_o$  is lithospheric thickness;  $Ar$  is Argand number, equal to  $[g\rho_c (1 - \rho_c/\rho_m)L_o^2]/\eta_o u_o$ ;  $\eta_o$ ,  $u_o$  are reference viscosity and velocity, respectively. In addition to the Navier-Stokes equation, the time-dependent continuity equation is also considered:  $\dot{S} = -S\nabla \cdot u$  (horizontal strain rates are accommodated by changes in crustal thickness).

[13] In the Navier-Stokes equations, tectonic force applied at the boundary is balanced by body force associated with crustal thickness gradients. The degree of balance is a direct function of the Argand number ( $Ar$ ) and the effective viscosity of the medium. In this modification of the original thin viscous approach the traction at the base of the lithosphere in the forearc region is incorporated as a new body force. Considering the proposed conceptual model, the traction at the interplate contact is expressed in terms of the slip parameter and the corresponding velocity component:  $\tau_{iz} = \eta_{\text{slip}} u_i / L_{\text{slip}} = 10 \{u, v\} \eta_{\text{slip}} / L_o$ .

[14] The problem is solved using the PDE2D6.0 package for finite element partial differential equations, using sparse lineal system solvers, with 3000 triangular elements, and cubic element types. Material properties and boundary conditions are described in Figure 2b. Mesh geometry considers a hypothetical initial configuration of the margin tilted in the NW direction. Effective viscosity of the continental lithosphere is characterized by the four domains described in section 2.2. For the slip layer viscosity we consider the end-members numbers of  $5 \times 10^{19}$  and  $5 \times 10^{20} \text{ Pa s}$ , which represent high and low interplate coupling. Given its low effective viscosity, the arc-foreland domain

**Table 1.** Convergence Rate and Dip Angles for the Transects Defined in Figure 2

Profile	Profile Latitude	Normal Convergence Rate, cm/yr	Age at the Trench, Myr	Near Trench Dip Angle, deg	Asthenosphere Dip Angle, deg	Reference for Dip Angle
15	3°N	5.2	13	17	43	<i>Gutscher et al.</i> [1999]
14	0°S	5.5	11	19	6	<i>Gutscher et al.</i> [1999]
13	4°S	5.9	30	17	22	<i>Gutscher et al.</i> [2000]
12	7°S	6.1	28	18	8	<i>Gutscher et al.</i> [2000]
11	11°S	6.4	29	20	7	<i>Gutscher et al.</i> [2000]
10	15°S	6.7	38	21	39	<i>Gutscher et al.</i> [2000]
9	18°S	7.0	43	21	44	<i>David et al.</i> [2002]
8	21°S	7.1	47	23	44	<i>David et al.</i> [2002]
7	24°S	7.3	45	23	36	<i>Gutscher et al.</i> [2000]
6	28°S	7.6	39	24	9	<i>Pardo et al.</i> [2003]
5	33°S	7.8	35	24	32	<i>Pardo et al.</i> [2003]
4	35°S	7.9	33	22	38	<i>Pardo et al.</i> [2003]
3	41°S	8.2	22	16	38	<i>Gutscher et al.</i> [2000]
2	46°S	8.2	0	13	25	<i>Jarrard</i> [1986]
1	52°S	2.7	14	13	40	<i>Rubio et al.</i> [2000]

concentrates the deformation, its width is set up constant along the convergent margin (1 unit = 100 km in the numerical model), but in practice, it is highly likely that it varies along strike. For instance, in flat slab segments [e.g., Yáñez *et al.*, 2002] it is likely narrower and further inland.

[15] Model response will be discussed in section 6, within the framework of the long-term Cenozoic evolution of the active margin of South America. However, previously, we have determined the appropriate parameters of the plate coupling for the Andean convergence. In order to do so, we have to determine the slip layer viscosity that equilibrates the present topography along the trench.

### 3. Present-Day Plate Coupling From the Dynamic Equilibrium of the Trench Topography

[16] Negative free-air gravity anomaly along convergent margins [e.g., *Smith and Sandwell*, 1994] demonstrates that this first-order topographic feature is not compensated isostatically. *Wdowinski* [1992] clearly shows that plate margin topography is the result of a dynamic equilibrium between two competing forces: (1) the tectonic force pulling the overriding plate downward and (2) body or buoyant force acting in the opposite sense (see details of this model in Appendix A). From *Wdowinski* [1992] the dynamic trench topography is controlled by three factors: The Grashof number, the slip layer parameter, and the dip angle of the Benioff plane. The Grashof number is the ratio of the buoyancy and tectonic forces, and it is mostly controlled by the overriding plate viscosity and the convergence plate velocity. The slip layer parameter is the ratio of the slip layer viscosity and thickness. If multiplied by the convergence velocity, it represents the interplate coupling in terms of the stress transferred to the continental plate. In the Andes, plate velocities and dip angles are fairly well constrained, whereas the slip layer parameter and the continental plate viscosity are poorly known. Kinematic plate models, such as NUVEL-1 [*DeMets et al.*, 1994], provide a good control of the along-strike variations of the convergence velocity. Dip angle of the Benioff plane can be determined from different seismological studies [*Gutscher et al.*, 1999, 2000; *David et al.*, 2002; *Pardo et al.*, 2003; *Rubio et al.*, 2000] or extrapolated from empirical relations

[*Jarrard*, 1986]. The dip angle of the Benioff plane is not regular; in fact, in the Andes, it is possible to identify two different angles, the near-trench dip angle (from the trench down to the base of the continental lithosphere), and the asthenosphere dip angle downward. Given the null role played by the asthenosphere in *Wdowinski's* formulation, the angle that matters is the near-trench dip angle. In Table 1 we include the dip angles and convergence velocities for the 15 transects defined to examine the plate coupling along the Andes, also included in Table 1 are the oceanic plate age at the trench (its relevance will become evident later on). As we pointed out in section 2, the near-trench overriding plate viscosity at the dynamic equilibrium is, to a first-order approximation, constant along the Andean margin. Therefore we can isolate the plate coupling problem by determining the along-strike variations of the slip layer parameter, with a constant overriding plate viscosity and a given slip layer thickness of 10 km. We ran a series of experiments using a wide range of overriding plate viscosities ( $1\text{--}5 \times 10^{22}$  Pa s) finding that the equilibrium slip layer viscosity is essentially insensitive to variations in the strength of the continental plate. Overriding plate viscosity will become important in the given rate to reach the dynamic equilibrium, being larger when the overriding plate viscosity is smaller. From *Wdowinski* [1992], trench topography equilibrium is reached after 5–10 Myr, after the onset of subduction regime starting from a flat relief. Therefore it is fair to assume that trench topography is essentially in quasi-static equilibrium, although subduction of active or passive ridges may locally perturb this assumption. Considering published estimates [*Wdowinski and O'Connell*, 1990; *Daniel et al.*, 2001], we adopted an average of  $10^{22}$  Pa s for the overriding plate viscosity.

[17] In the following approach, the corresponding equilibrium slip layer viscosity is the one capable of reproducing the observed dynamic trench topography in each transect defined in Table 1. Details of the modeling technique are shown in Appendix A. The model of each transect proceeds in the following way: We fixed the slip layer thickness in 10 km and incorporated the corresponding convergence velocity and dip angle from Table 1 and the trench topography from Figure 3. With these parameters we computed the velocity field of the

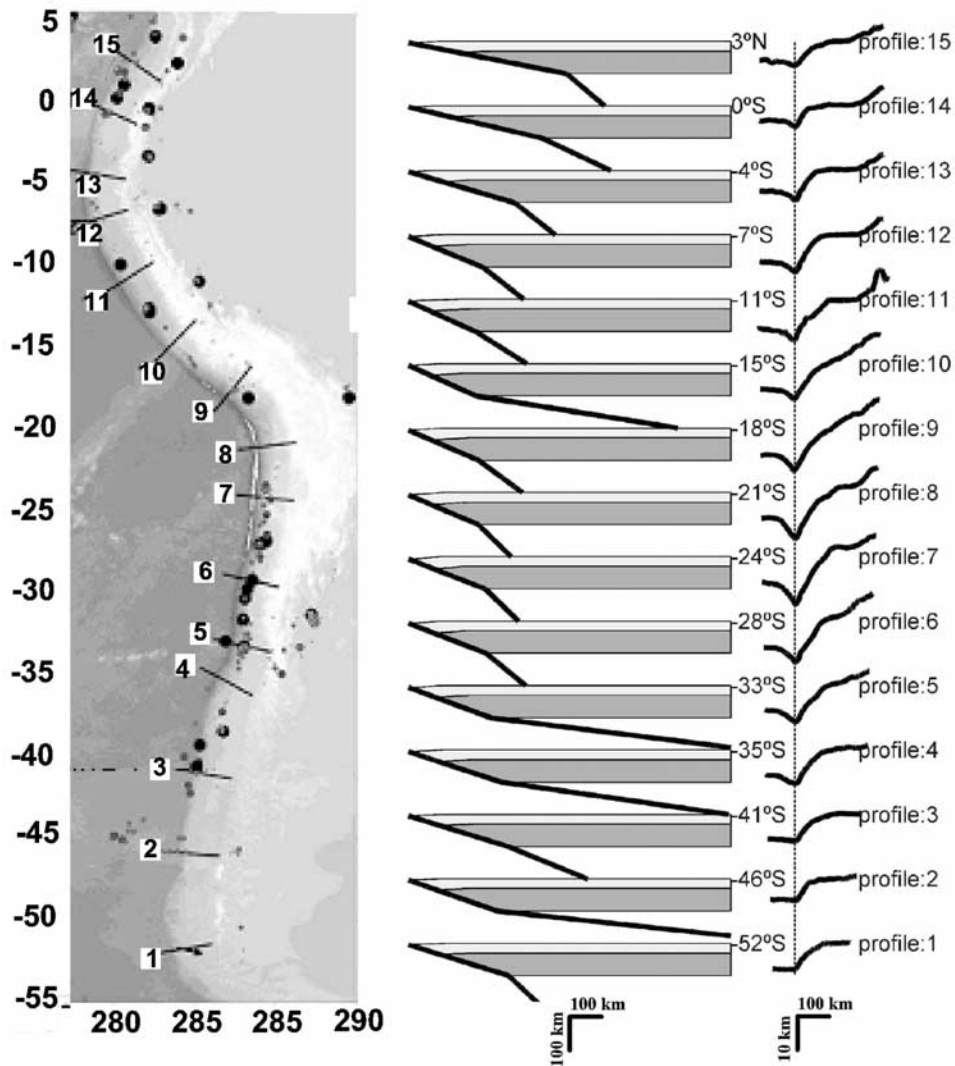


**Figure 3.** Trench topography for 15 profiles along the Andes between 3°N and 56°S. (left) Topography/bathymetry from *Smith and Sandwell* [1994], overlapped by the shallow seismicity (0–30 km) for the 1970–2000 period (extracted from the Data Center Council of the National Seismic System database). (middle) Dip of the Benioff plane at 1:1 scale. (right) Topography/bathymetry profiles derived from the 15 sections analyzed with an enhancement of 10 in the vertical axes (see details in Table 1).

overriding plate for a range of slip layer viscosities (between  $0.003$  and  $0.03 \times 10^{22}$  Pa s). If the slip layer viscosity is too small, buoyancy force dominates, and the flow field is trench-orthogonal and upward. In contrast, for a large slip layer viscosity, tectonic force dominates, and the flow field is trench-orthogonal but downward. Therefore the equilibrium slip layer viscosity is the one that achieves the smaller flow field for the range of computed slip layer values. Figure 4 shows the model results for three selected transects. In the three cases we see how the flow field converges to a minimum amplitude for a given slip layer viscosity. In some profiles the minimum velocity field is better achieved than in others, probably as a consequence of a better equilibrated dynamic trench topography.

[18] In Figure 5 we summarize the model results in terms of the equilibrium slip layer viscosity for all transects. In Figure 5 the convergence velocity and the age of the subducting plate also are shown for further correlation.

[19] The model results from the equilibrium of the dynamic trench topography along the central and southern Andes shown in Figure 5 indicate that the viscosity of the slip layer varies along strike of the trench axis in the range of  $0.45$  to  $2.1 \times 10^{20}$  Pa s. According to the modeling effort the slip layer viscosity shows a direct correlation with the age of the subducting slab in the Nazca Plate. Somewhat surprisingly, the lowest coupling is spatially associated with the active ridge collision zones at the Taitao Triple Junction (TJ) and the Carnegie Ridge. On the other hand, the oldest oceanic crust near the Arica elbow (45 Ma) shows the maximum slip layer viscosity. Passive ridges, contrary to the common belief [e.g., *Gutscher et al.*, 1999], do not show large slip layer viscosity numbers; in fact, there is a tendency toward smaller values than the surrounding areas (the most remarkable case is that of profile 15 at the Carnegie Ridge subduction). This first-order age correlation with



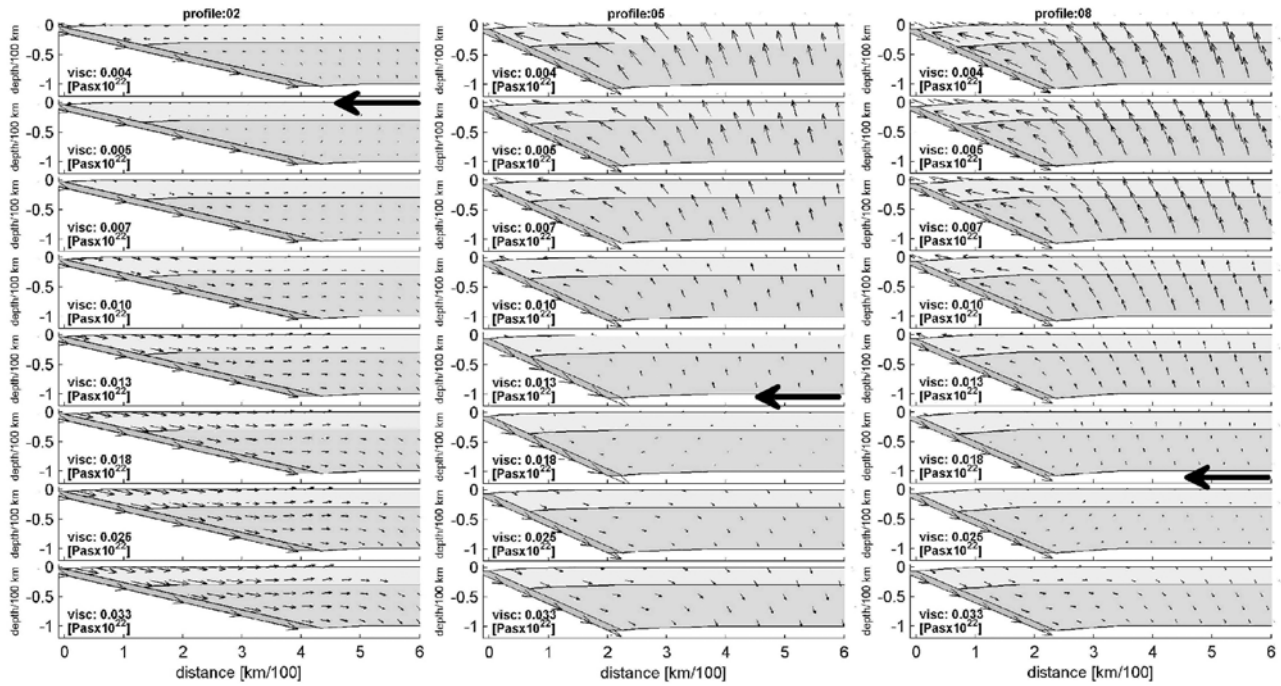


**Figure 4.** Dynamic trench topography modeling for profiles 2, 5, and 8 (described in Figure 3 and Table 1). The flow field for a given trench topography and near-trench dip angle of subduction, considering different slip layer viscosities (from  $0.004$  to  $0.033 \times 10^{22}$  Pa s) are shown. The solid arrow indicates in each case the slip layer viscosity of minimum flow field (the equilibrium slip layer viscosity). Crust, mantle, and slip layer are represented by with different shading.

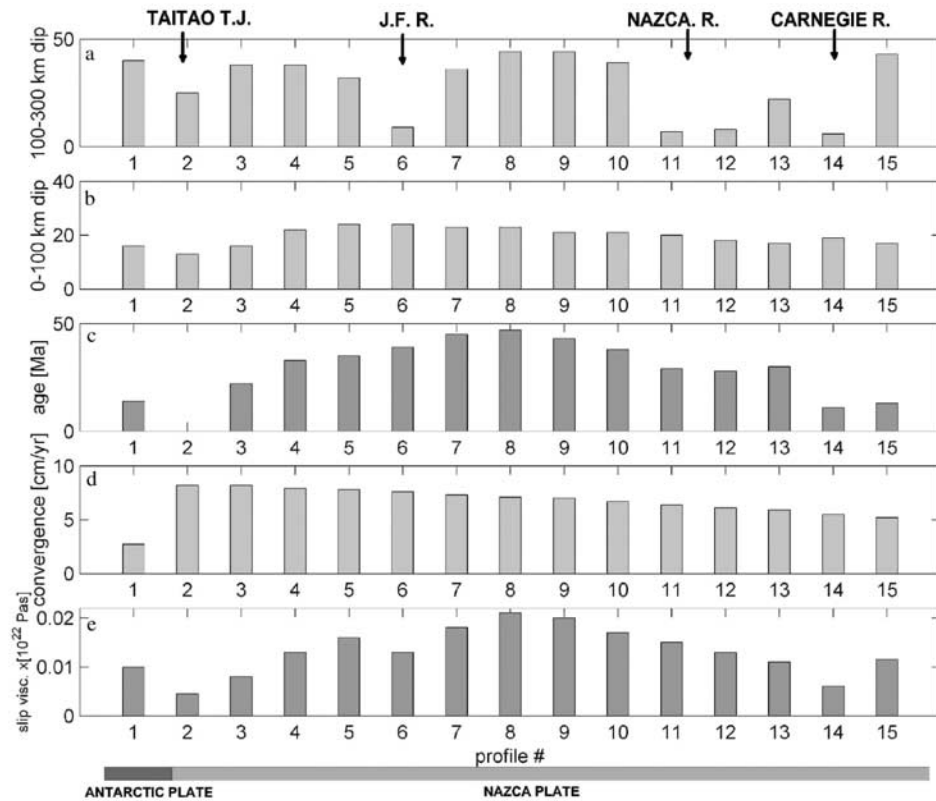


**Figure 5.** Model results. (a) Slab dip under the asthenospheric wedge. (b) Near-trench slab dip angle. (c) Age of the subducting slab at the trench. (d) Convergence velocity. (e) Slip layer viscosity for a slip layer thickness of 10 km. The profile numbers are indicated at bottom, and their spatial location is displayed in Figure 3.



the slip layer viscosity suggests that relative coupling reduction of passive ridge subduction implies a thermal (age) resetting in those zones.

[20] The thermal (age) dependence of the plate coupling is developed in detail in the next section, providing an empirical rule to determine the resistance at the slip zone as a function of the oceanic plate age at the trench and the convergence velocity. This result is used in section 5 in the 2.5-D deformation modeling for the Late Cenozoic evolution of the Andean margin.

#### 4. Thermal and Strain Rate Dependence of the Plate Coupling

[21] The slip layer age dependence described in section 3 suggests a significant thermal influence in the rheology of the weak coupling between the oceanic and continental lithosphere. The thermal field at subduction zones has been thoroughly reviewed by different authors [e.g., *Davies and Stevenson, 1992; Daniel et al., 2001*]. Following *Davies and Stevenson's* [1992] formulation, we investigated the thermal field at the slip layer zone, varying the age and the convergence rate according to the constraints of the present Andean convergence. Details of the modeling technique are described in Appendix B.

[22] The strength of the slip layer zone is the result of two competing mechanisms [e.g., *Ranalli, 1995*]: (1) brittle behavior at shallow levels (low temperatures) [ $\Delta\sigma_b$ ], and (2) dislocation creep under high-temperature regimens [ $\Delta\sigma_d$ ]. Details of both deforming mechanisms are given in Appendix C. The strength of the slip layer zone at a certain depth is given by minimum energy condition ( $\Delta\sigma = \min(\Delta\sigma_b, \Delta\sigma_d)$ ). The yield strength for the whole slip zone of length  $L_s$  will be

$$\sigma_y = \frac{1}{L_s} \int_0^{L_s} \Delta\sigma_s dz.$$

Using the corresponding thermal gradient and convergence velocity, the yield strength envelope for each profile of Figure 3 was determined. Results of this computation are shown in Figure 6a. Obtained yield strength envelopes confirm the expected result of a larger strength in older transects (e.g., profiles 8 and 9). As pointed out by several authors [e.g., *England, 1983*], the strength is largely controlled by the strength of the mantle rheology, when the isotherm is sufficiently low. To compare this theoretical formulation with the observed slip layer viscosities, we computed the effective viscosity by the following approximate formula [e.g., *Ranalli, 1995*]:  $\eta_{\text{comp}} \approx \sigma_y/2\dot{\epsilon}$ . In Figure 6b (top) we compare the equilibrium slip layer viscosity and the computed effective viscosity. Despite the limitations and simplicity of the proposed model, the agreement between observations and theory are quite remarkable. In Figure 6b (bottom) we compare the observed strength of the slip layer (derived from the product of the slip layer parameter and the convergence velocity) and the computed yield strength. Again, both curves agree quite well, showing a maximum of  $\sim 100$  MPa for older oceanic crust (profiles 8 and 9) and a minimum  $<20$  MPa for

young oceanic crust (profiles 1–3). This stress range represents a direct measure of relative plate coupling at the Wadatti-Benioff region, which is in good agreement with natural stress estimates obtained from different lines of reasoning [e.g., *Scholz and Campos, 1995; Molnar and England, 1990; Froidevaux and Isacks, 1984*].

[23] Major controls on the strength of the slip layer are the mantle flow law, the temperature at the Moho, and the strain rate [*England, 1983*]. According to *England* [1983] the depth-integrated strength of a power law material will be proportional to  $\dot{\epsilon}^{1/n} T_m \exp(A/nRT_m)$ , where  $T_m$  is the absolute temperature at the mantle. In our problem this proportionality implies the following dependence with the convergence velocity and the age of the oceanic crust at the trench  $\approx CV^{1/4} \text{age}^\alpha$ , where  $C$  and  $\alpha$  are constants to be determined. A simple regression was performed on the 15 profiles of Figure 3, obtaining the following empirical relationship for the slip layer strength:  $\sigma_{\text{slip}} [\text{MPa}] = 0.58 V^{1/4} \text{age}^{1.22}$ , where  $V$  is given in cm/yr and age is given in Myr. This empirical relationship was tested by evaluating its response at each profile along the Andes. Model results shown in Figure 6b (bottom) indicate the good correspondence of this empirical relationship and observations. In Figure 6c we show a theoretical response of this empirical strength of the slip layer in terms of a family of plate velocities and age at the trench. Figure 6c shows clearly that major control on the slip layer strength is the age of the oceanic crust at the trench, ranging from  $<20$  MPa to  $>100$  MPa in a time span of 50 Myr, whereas velocity dependence only becomes important for age at the trench greater than 30–40 Myr. Figure 6c also shows the effective viscosity at the slip layer considering a slip thickness of 10 km. In this case the slip resistance is larger for older oceanic crust but more dramatic with a decrease in the convergence velocity, given the fact that the effective viscosity is inversely proportional to  $V^{3/4}$ . The empirical relationship obtained in this section is used in section 7 as the resistance force for the 2.5-D deformation model of the Andes. Given the age and velocity dependence of this resistance force, in section 5 we estimate the appropriate parameters for the late Cenozoic evolution of the Andean margin.

#### 5. Nazca Plate Age at the Trench and the Associated Slip Layer During the Late Cenozoic

[24] A significant fraction of the present-day Andean relief is definitively younger than  $\sim 25$  Ma [*Muñoz and Charrier, 1996; Baby et al., 1997; Jordan et al., 2001; Muller et al., 2002*]; therefore, using this time window we have the chance to test the model against the basic observation of the Andean relief evolution. In order to apply the slip layer approach to constrain the plate coupling in the long-term evolution of the Andean orogenesis, we need to know temporal variations of the convergence velocity and age at the trench. This task cannot be fully addressed for two reasons. The age of the oceanic crust at the trench prior to 25 Ma is poorly constrained because relevant isochrons have been already subducted. In addition, given the deformation of the margin, it is highly likely that the shape of the continental

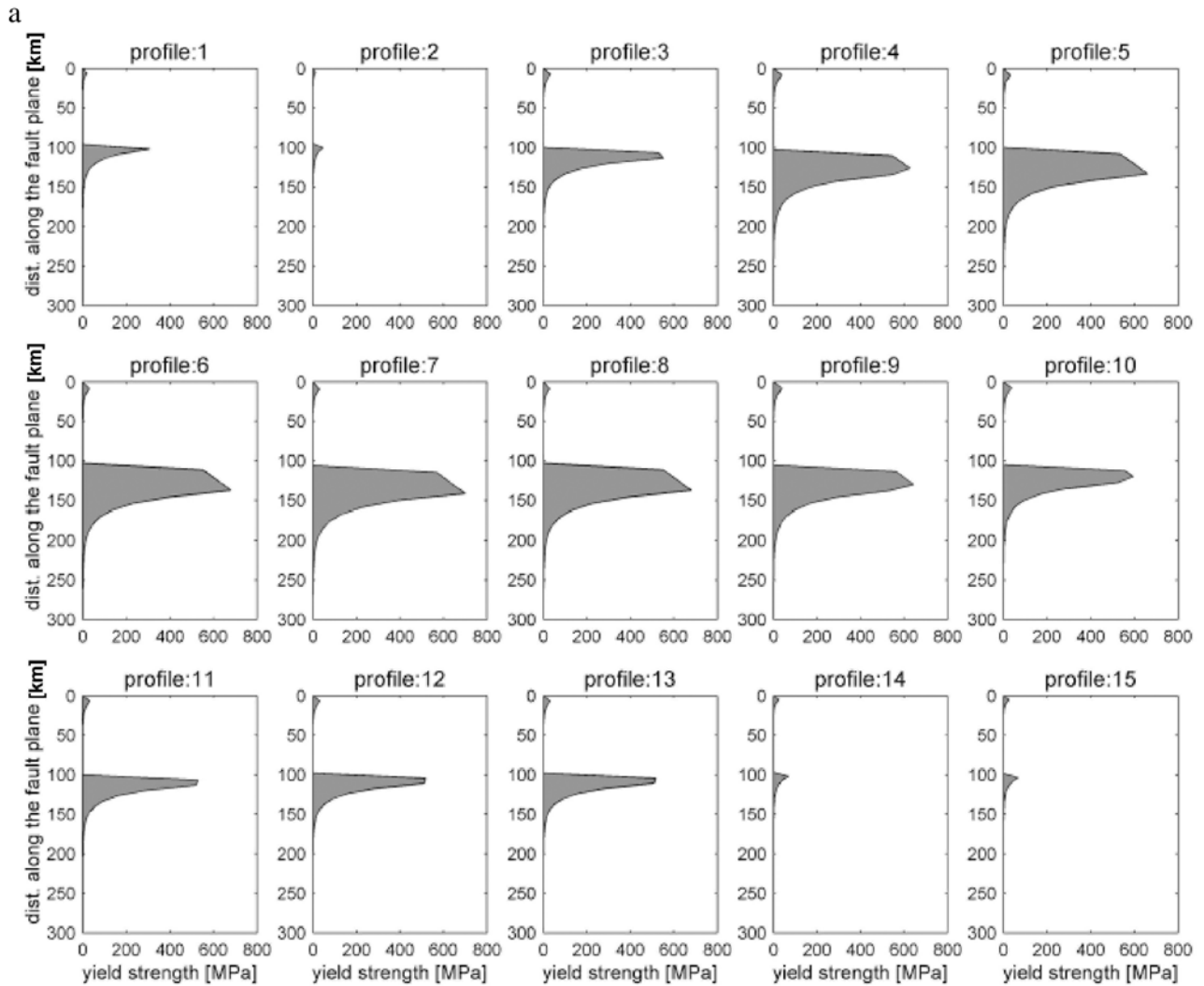


**Figure 6.** (a) Yield strength envelope along the slip plane for the 15 profiles defined in Figure 3. (b) (top) Comparison between the observed and computed slip layer viscosities. (bottom) Same results as Figure 6b (top) (but expressed in terms of the fault strength). We also include the empirical model response of the fault strength (light heavy line). (c) Empirical model response. (top) Fault strength and (bottom) slip layer viscosity for a family of convergence velocity and age of the oceanic plate at the trench.

plate has been modified with time. Despite these limitations, we can attempt a rough estimate of the oceanic plate age and velocity at the trench, considering the absolute and relative plate reconstruction for the Late Cenozoic [Gordon and Jurdy, 1986; Somoza, 1998] and a backward extrapolation of present-day magnetic isochrons [Tebbens and Cande, 1997]. The absolute poles of rotation and angular velocities for Nazca/Farallon-Antarctic and South America plates used in the plate reconstruction are given in Table 2. Margin plate age reconstruction for the last 25 Myr is shown in Figure 7. The main characteristic of this reconstruction is the age segmentation, with a relatively old central segment facing the Altiplano zone (older than 50 Ma), and a transition to younger oceanic crust both northward and southward. This transition toward younger oceanic crust has a greater slope north of the Altiplano. However, the southern segment increases its age gradient south of 35°S, where there is a large age contrast across the Challenger Fracture Zone. Looking backward in

time, the age at the trench exhibits two important transient behaviors. The central, old segment reduces its N-S wavelength in >400 km in the last 25 Myr. On the other hand, the northward motion of the Taitao TJ (see present location in Figure 1) conditions a progressively decrease in the age at the trench northward and an increase southward. As we will discuss in section 7.2, these transient phenomena may have important implications in the forearc evolution of the margin. In the same time period (25–0 Ma), the Nazca-South America convergence velocity shows an almost steady 40% decrease, from 14 to 8 cm/yr. A second-order feature of the Nazca-South America plate interaction is the 20% northward reduction in convergence rate, which is even higher at 25 Ma, whereas to the south of the Taitao TJ, the Antarctic-South America convergence is kept essentially constant at rates in the order of 2 cm/yr.

[25] The age-dependent convergence velocities and plate age at the trench, shown in Figure 7, are introduced into

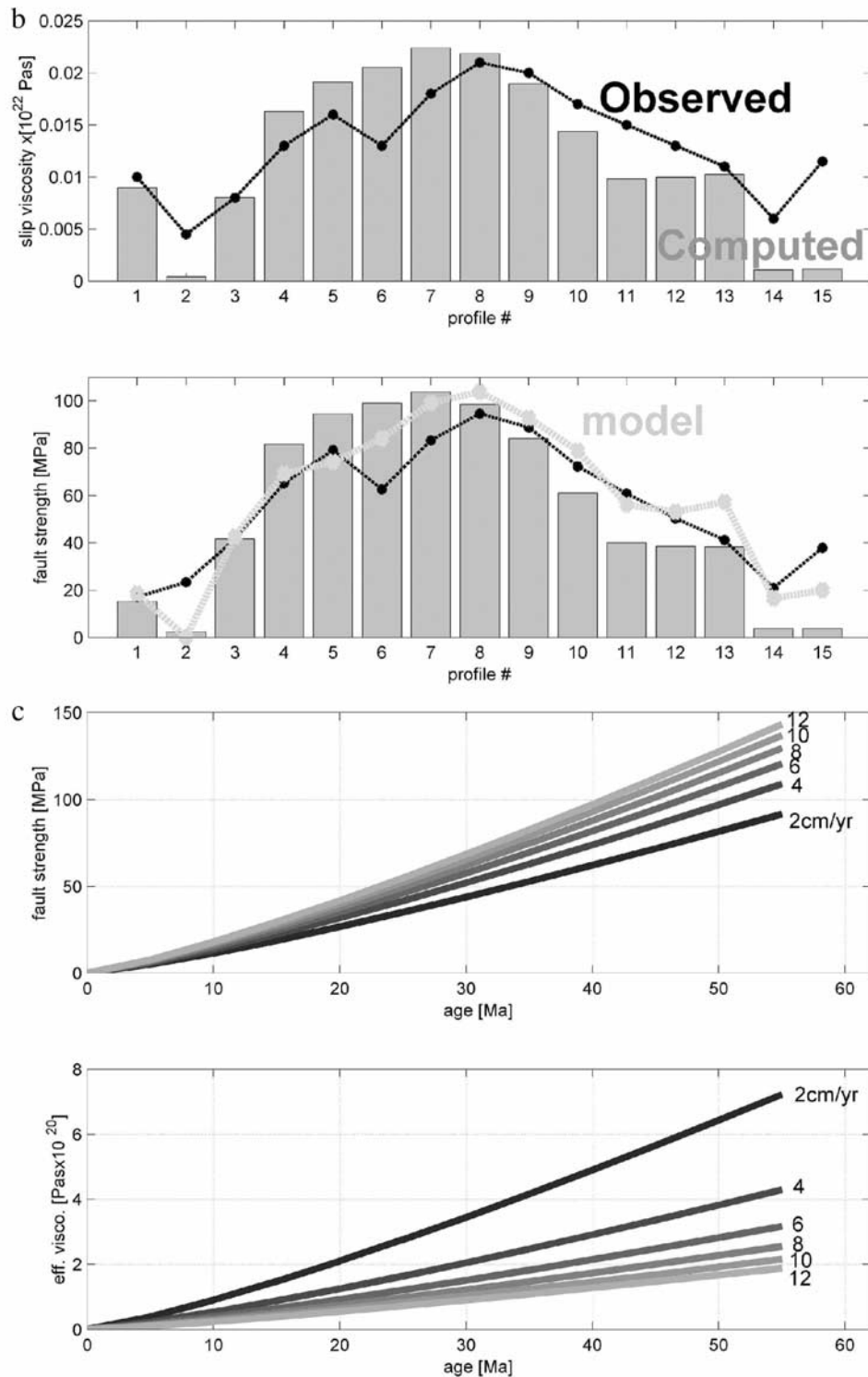


Figure 6. (continued)

the empirical relationship derived in section 4 in order to determine the time and space varying slip layer strength along the Andes. The computed slip layer strength is also included in Figure 7. One important feature of these parameters is the greater sensitivity to high temperatures, and therefore the transition from old to young oceanic plate age is more dramatic than in the opposite direction.

One important characteristic of the slip layer viscosity shown in Figure 7 is the concentration of high values between latitudes 18 and 28°S, roughly coincident with the Altiplano and Puna region (Figure 1). Such high viscosity values are restricted to the last 10–15 Myr, suggesting a stronger coupling focused on this region in the late Tertiary only. The obtained slip layer strength will



**Table 2.** Poles of Rotation and Angular Velocities for Nazca/Farallon and South American Plates

Time, Ma	Nazca/Farallon Plate			South America Plate		
	Latitude, deg	Longitude, deg	Velocity, deg/Myr	Latitude, deg	Longitude, deg	Velocity, deg/Myr
64	-26	-62.7	-1.08	41.8	52.4	-0.308
56	-50.4	-27	-1.266	58.8	47.7	-0.297
48	-40.6	-51.8	-1.026	78.9	43.8	-0.392
43	-43.8	-26.6	-0.694	77.6	26.8	-0.187
25	-57.5	80.1	-0.742	80.5	-12.9	-0.119
10	-47.4	84.2	-0.856	79.1	-15.7	-0.113

be used as boundary conditions in the long-term deformation modeling of section 6.

## 6. Long-Term Deformation Evolution of the Andean Margin

### 6.1. Synthetic Slip Layer Viscosity Boundary Condition

[26] In order to gain some insights on the model response, modeling results are first carried out for a prescribed slip layer distribution. Figures 8a–8c show the 28–0 Ma time-dependent 2.5-D arc-foreland deformation for a slip layer viscosity transition, from low to high plate coupling, that resembles the transition from young (~0 Ma) to old (~60 Ma) oceanic plate age at the trench. Despite the roughness of the model, we can distinguish some interesting features of the deformation process. At

the beginning, the shortening velocity is maximum for both end-member coupling zones (Figure 8a). When continental crust thickens in the highly coupled zone, the associated buoyancy force starts to counterbalance the shortening velocity. At this point the forearc velocity ( $U_{FA}$ ) approaches the continental plate velocity ( $U_{SA}$ ), increasing in this way the trenchward motion of the overriding plate. The differential shortening velocity across the transition zone implies strike slip displacement, with right-lateral or clockwise sense of displacement in this case. In addition, when the crust thickens (Figure 8b), the outflow from buoyant zones (thickened crust) migrates to low relief zones, with a more trench parallel deformation. The strain rate (Figure 8c) is highly compressive at the beginning of the experiment, with numbers in the order of the observed deformation in the Andes. However, as long as the crust thickens, negative strain rate is reduced and concentrated into the transition to the cratonic region. The differences in age-dependent slip layer viscosities imply a concave shape of the margin for subduction of old oceanic crust, like in the Altiplano orocline. Conversely, for subduction of young oceanic crust the margin shape approaches a convex form, like in the Taitao Triple Junction in the southern Andes.

### 6.2. Age-Dependent Slip Layer Viscosity Boundary Condition

[27] The strength of the slip layer, expressed empirically in terms of the age at the trench and the convergence

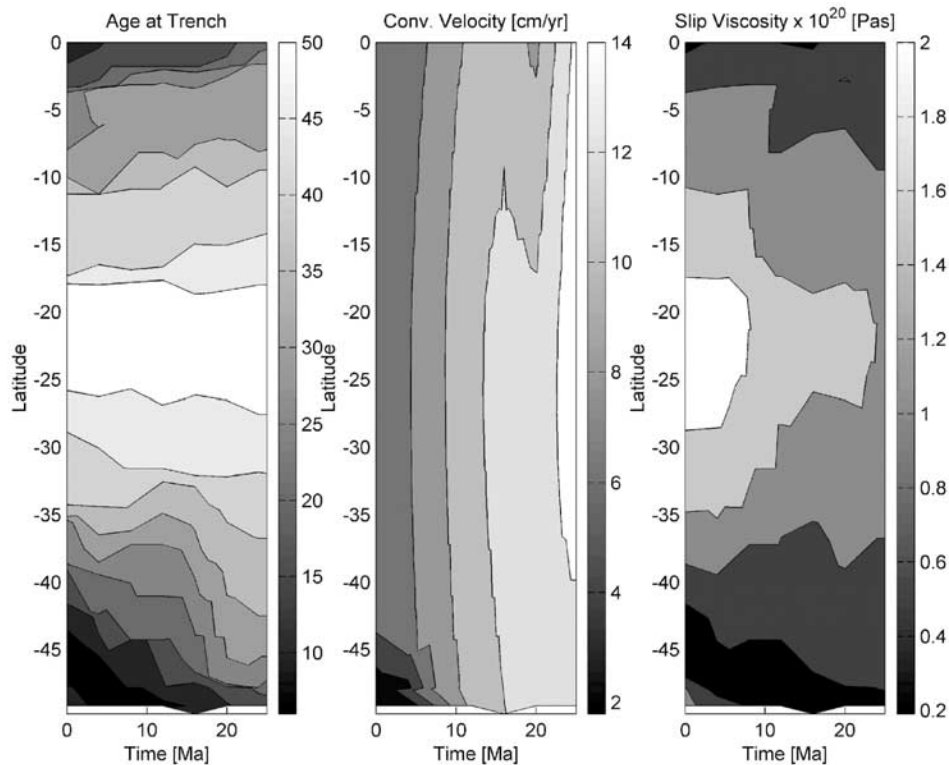


**Figure 7.** Age, convergent plate velocity, and slip layer viscosity at the margin for a time window of 0–25 Myr. (left) Oceanic plate age at the trench. (middle) Convergence velocity. (right) Slip layer viscosity. Horizontal axis corresponds to the time at which these parameters are evaluated. Vertical axis is the latitude of the plate margin.

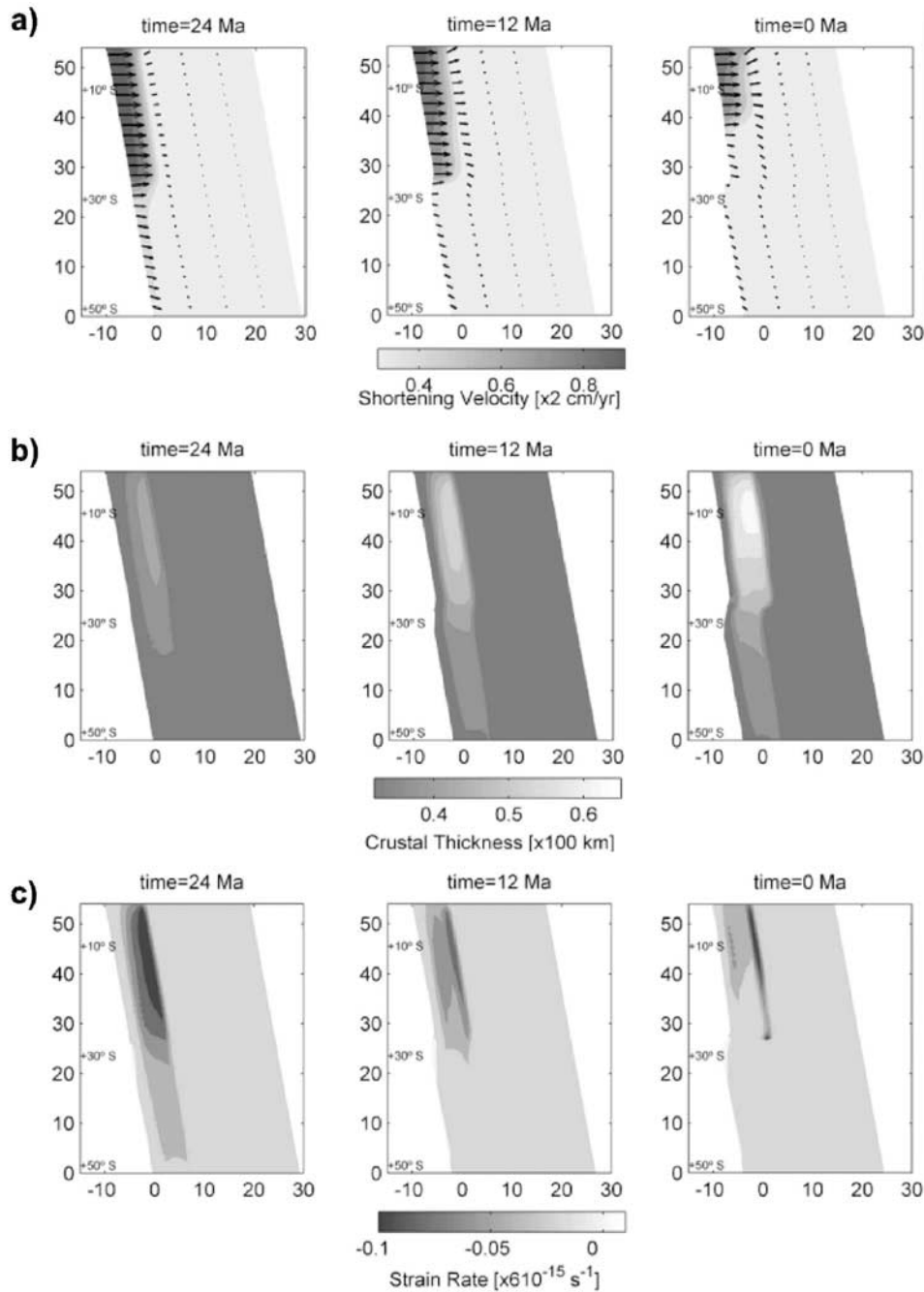


**Figure 8.** Long-term deformation modeling considering a simple distribution of low slip layer viscosity ( $2 \times 10^{19}$  Pa s) in the lower half and a high slip layer viscosity ( $2 \times 10^{20}$  Pa s) in the upper half. The modeling starts at 28 Ma with an initial crustal thickness of 33 km. Model results are shown for 24–12 and 0 Ma. One horizontal and vertical unit represents 100 km. The space window selected in this model represents the South American plate between  $-55^\circ\text{S}$  to  $0^\circ\text{S}$ . (a) Flow velocity shown in terms of absolute contours and flow field in white arrows. (b) Crustal thickness. (c) Principal strain rate. Compression is shown in dark gray and extension (or transtension) in light gray.

velocity (section 5, Figure 7), is used now as a boundary condition to run a numerical experiment for the long-term deformation of the active margin. Initial conditions for some poorly known parameters, like the shape of the margin, the crustal thickness, and the width of the deforming zone, are kept as simple as possible in order to minimize their influence on the model output. We chose a margin with a

linear slope of  $-20\%$  N-S, trying to resemble the first-order trend of the present-day margin. Crustal thickness and its along-strike variation are very important for the buoyancy force condition, and some lines of reasoning indicate a relatively thin crust during the early Miocene [e.g., *Isacks*, 1988; *Gregory-Wodzicki*, 2000; *Jordan et al.*, 2001]. In the models we fixed the initial crustal thickness to a constant

number of 33 km. The width of the deforming zone is probably linked to the asthenospheric wedge underneath [e.g., *Isacks*, 1988] and the spatial distribution of a more competent cratonic zone eastward. The development of a warm asthenospheric wedge depends on the dip of the subducting slab [e.g., *Gutscher*, 2002]. Flat slab segments are present in the northern and central part of the study area (north of the Arica elbow at 18°S, in association with the Nazca and Carnegie Ridge subduction; and between 28 and 33°S linked to the subduction of the Juan Fernandez Ridge). In addition, the southward migration of the Juan Fernandez Ridge and the associated flat slab segment [*Yáñez et al.*, 2001, 2002] introduces a time-dependent thermal perturbation that must be considered in more thorough studies. The shape of the western edge of the craton is less clear, although geological evidences [e.g., *Jordan et al.*, 2001; *Lamb and Hoke*, 1997] suggest a wider preexisting foreland basin in the Altiplano region in comparison to the southern segments. We chose a 600-km-wide constant deforming zone along the entire margin, trying to resemble the initial conditions of the Altiplano-Eastern Cordillera region, the better constrained and more outstanding segment of the central Andes. In this initial attempt to understand the main driving mechanism of deformation along the margin, perturbations associated with the episodic effect of flat slab segments were not considered. The remaining parameters of the problem, such as the effective viscosities of the over-riding lithosphere, were kept with the same values as in the previous experiments: 5, 1, and  $100 \times 10^{22}$  Pa s for the forearc, arc-foreland, and cratonic-oceanic segments, respectively. The “ridge push” (Atlantic Ridge) velocity was kept constant at 2 cm/yr, in agreement with the mean plate velocity in a hot spot reference frame [*Schult and Gordon*, 1984] for the same time span. The problem is solved numerically, considering a time span of 28 Myr. Model results are presented in Figures 9a–9c.

[28] Shortening velocities of Figure 9a indicate an E-W flow pattern in early times, progressively reduced as the crust thickens later on (Figure 9b). Shortening rates are higher in the Altiplano region and decrease to the north and south. Shortening rates in excess of 1.2 cm/yr are later on reduced to <0.8 cm/yr. Reported shortening rates for the Altiplano-Eastern Cordillera region are in the order of ~200 km for the last 25 Myr [e.g., *Isacks*, 1988; *Lamb and Hoke*, 1997; *McQuarrie*, 2002a; *Muller et al.*, 2002]. This means a roughly average of 1 cm/yr, in agreement with model predictions. In the central zone at 30°S, *Ramos* [1985] and *Jordan and Allmendinger* [1986] reported ~100 km/25 Myr, which is also comparable with a mean value of 0.5 cm/yr obtained in the models. From the discussion by *Jordan et al.* [2001], we can infer a rate less than 50 km/25 Myr in the southern Andes, again in good agreement with model predictions in the order of 0.2 cm/yr.

[29] When the crust thickens (Figure 9b), the increment of the buoyancy forces induces a clockwise rotation south of the high relief Altiplano region and counterclockwise northward, in good agreement with paleomagnetic data on rotations affecting late Tertiary ignimbrites of the region [e.g., *Roperch et al.*, 2000]. Rotation becomes more pronounced as a direct result of escape tectonics associated with buoyancy forces. In the southern segment the progressively younger oceanic crust at the trench and the associated

reduction in the slip layer viscosity induce a nearly north-south flow in the deforming zone, with an almost fixed forearc region (latitude 40–50°S). Such a flow pattern can be interpreted as a right lateral arc-parallel displacement, in good agreement with well-documented Late Cenozoic intra-arc deformation at the southern Andes [*Lavenue and Cembrano*, 1999; *Cembrano et al.*, 2000]. In recent times (8–4 Ma) the forearc region of the southern segment shows a southwestward flow which is also reflected in the strain rate pattern of Figure 9c as transition from negative (transpression) to slightly positive (transtension) domain (the first 2 units = 200 km, at latitudes 40–50°S). This transtensional domain is spatially correlated with the Central Depression of the forearc region south of 33°S.

[30] The crustal thickness of Figure 9b is in good first-order agreement with the observed margin relief and shape. Certainly, the observed bending at the Arica elbow (20°S) is much more pronounced than the one predicted by the model. However, the model run for a period of 28 Myr only, but the ridge push force from the South Atlantic Ridge was active for at least four times during this time window. During the early Tertiary, mean velocity of the continental lithosphere almost doubled the present level of 2 cm/yr [*Schult and Gordon*, 1984], predicting a much stronger shortening at that time. This argument is supported by restorations of the Bolivian orocline implying total shortening amounts in excess of 500 km for the last 50 Myr [*McQuarrie*, 2002b]. In addition, *Somoza* [1998] shows that convergence rate prior to 28 Ma is considerably lower than present rates, indicating a much stronger coupling (see model predictions of Figure 6c). In fact, *Arriagada et al.* [2003] show that the Arica elbow was mostly produced during early Tertiary times.

[31] South of the Taitao Triple Junction (~45°S) we can also observe an incipient eastward bending as in the Tierra del Fuego Orocline. Crustal thickness in the Altiplano region reaches the present-day topography in the appropriate time span [e.g., *Isacks*, 1988; *Muñoz and Charrier*, 1996]. South of this region, there is a dramatic reduction in the crustal thickness and less focused relief than observed, probably as a direct response of the predefined wider deforming zone.

[32] The strain rate field of Figure 9c shows a pervasive compressive regime in the order of  $0.5 \times 10^{-15} \text{ s}^{-1}$  at early stages, in agreement with the average geological estimates for that time [e.g., *Hindle et al.*, 2002]. Later, the action of buoyancy forces tends to balance the tectonic forces, in this way reducing the compressional strain rate, which is then focused onto the eastern flank of the deforming zone. Active tectonism is, in fact, restricted to the Precordillera zone [e.g., *Dewey and Lamb*, 1992]. In contrast, the already mentioned extension in the southern flank is focused on the western flank of the deforming zone, with amplitudes 1 order of magnitude less than the compressive regime of the early stages ( $0.5 \times 10^{-16} \text{ s}^{-1}$ ). Implications of the model results are further discussed in section 7.

## 7. Discussion

[33] In this paper we developed a conceptual mechanism that tries to explain large-scale tectonic processes associated with Andean-type active margins. This mechanism is based



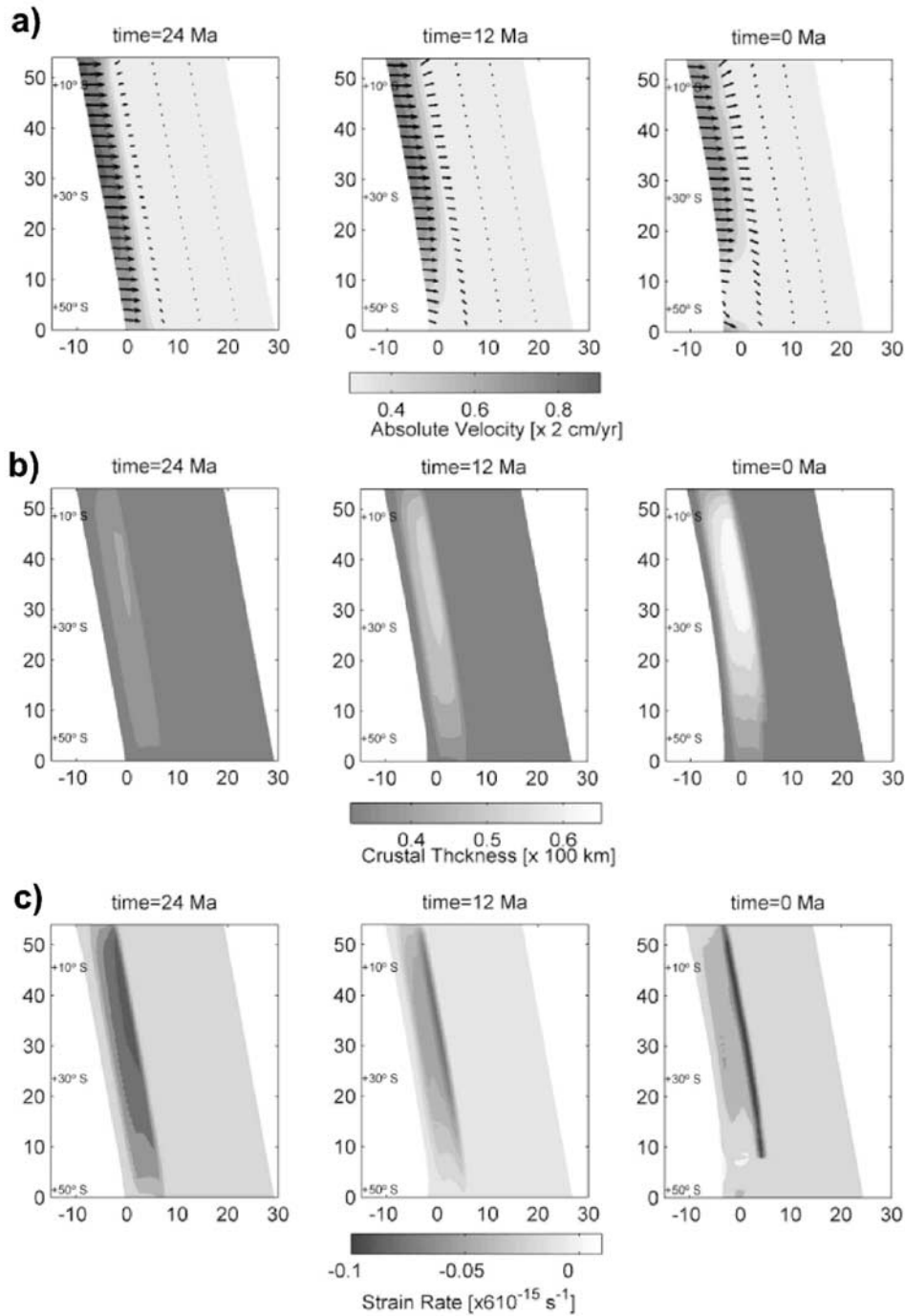


**Figure 9.** Long-term deformation modeling of the arc-foreland region of the active margin of South America for the last 28 Myr, using the slip layer viscosity derived in Figure 7. Details are the same as in Figure 8. (a) Flow velocity in terms of absolute contours and flow field in white arrows. (b) Crustal thickness. (c) Horizontal principal strain rate. Compression is shown in dark gray and extension (or transtension) in light gray.

on the concept of an age- and strain rate-dependent plate coupling. The derived strength of the plate coupling is on the order of 30–90 MPa, which is consistent with independent natural estimates in subduction environments. The numerical application of this mechanism enables us to predict some first-order features of the late Tertiary Andean evolution, among them, the formation of the Bolivian Orocline in the

proper time frame and the onset of counterclockwise and clockwise rotations to the north and south of the Arica elbow. In addition, the model provides a mechanism to explain oroclinal bending but considering timescales of several tens of million of years and mostly during the Late Cretaceous and early Tertiary in agreement with paleomagnetic results [Arriagada *et al.*, 2003]. The success of this conceptual

approach suggests its application to explain other relevant elements of the Andean geological record, which are beyond the time span and length scale analyzed in section 6.

### 7.1. Role of Convergent and Absolute Plate Velocity

[34] The proposed model splits plate convergence into its natural absolute plate velocities (hot spot referenced). Under this concept, oceanic plate velocity has two relevant effects: (1) it equilibrates the dynamic trench topography in time periods in the order of 5–10 Myr and (2) through the convergence velocity it modulates the resistance to the westward motion (and deformation) of the overriding plate. However, deformation of the continental margin can only be achieved if the “ridge push” from the Atlantic is present. Under this mechanism the resistance at the slip zone can either enhance or prevent the shortening process. Along-strike variations in age of the oceanic crust at the trench may explain also why the orogenic process has not been uniform and continuous during the Andean cycle [e.g., *Mpodosis and Ramos*, 1990]. Major cycles of deformation, including clockwise block rotations, have been described for the early Tertiary period in the Cordillera de Domeyko [*Arriagada et al.*, 2000], in agreement with a period of faster continental plate motion [*Schult and Gordon*, 1984] and slow Nazca-South America convergence in the early Tertiary [*Somoza*, 1998]. Furthermore, the pervasive clockwise rotation, in space and time, south of the Altiplano region during the Andean Cycle [*Beck et al.*, 1994; *Roperch et al.*, 2000; *Arriagada et al.*, 2000, 2003], can be interpreted in terms of the proposed model. A continuous process of southward escape tectonics may be triggered by a deformable segment in the Altiplano region and the quasi-steady presence of a relatively older oceanic crust at the trench.

### 7.2. Transient Evolution of the Forearc Region: Tectonic Erosion and the Development of the Present-Day Central Depression

[35] Tectonic erosion is an important issue in the building of the Andes. To the north of 33°S, the Meso-Cenozoic magmatic arc migration has been interpreted as a quasi-steady tectonic erosion of the margin [*Stern*, 1991]. Tectonic erosion at subducting margins requires high friction at the interplate zone [e.g., *Jarrard*, 1986]. However, the same segment that shows tectonic erosion to the north of 33°S is also affected by pervasive extensional tectonism in the coastal and offshore area [*González et al.*, 2003; *von Huene and Ranero*, 2003]. This apparent contradiction can be explained under the age- and strain rate-dependent slip layer mechanism. At least during the Tertiary, the northern segment of the Andean convergence zone shows a stronger coupling due to the older subducting plate at the trench and the slow down in the convergence velocity (Figure 7). In the framework of the model, large coupling implies larger downward bending and extension of the forearc region and at the same time larger compression in the arc-foreland region (see Figures 9a–9c).

[36] Another important first-order feature of the margin, probably associated with a transient evolution of the age at the trench, is the Central Depression to the south of 33°S. Figure 7 shows the progressive reduction in slab age because of the northward migration of the Taitao TJ. In the frame of the proposed model, two competing effects are

present in the late Tertiary tectonic evolution of the segment: (1) an increase in coupling due to the reduction in convergent velocity and (2) coupling reduction due to the younger oceanic crust at the trench. The age-dependent effect dominates in this case due to its grater sensitivity to very young oceanic crust (see discussion in section 4). Therefore the less resistive force at the slip layer in the southern Andes probably triggers a more effective forearc decoupling and growth of the Central Depression.

### 7.3. Reduction in Convergence Rate and the Inversion of Sedimentary Basin in the Southern Andes

[37] One key element when analyzing the orogenic process in the Andes is the role of the convergence velocity, which is often reduced to the fate of oceanic plate kinematics. However, different authors [e.g., *Jordan et al.*, 2001; *Hindle et al.*, 2002] have pointed out the lack of obvious direct correspondence between the geological record and oceanic plate kinematic history. In fact, in the southern central Andes the Oligo-Miocene volcanic deposits were accumulated during a period of high convergence rate, and later on uplifted when convergence decreased [*Jordan et al.*, 2001]. The proposed model can simply explain this behavior in terms of the strain rate and age dependence of the coupling. When convergence is high, the plate coupling is low as a result of the much younger oceanic crust at the trench and the associated high strain rate. This low coupling period, compared with the previous stages, favors an extensional regime (likely further incremented due to the vigorous asthenospheric flow) and the basin infill with volcanic products. When the convergence regime is modified to a much lower rate in the late Miocene, the opposite is predicted by the model, older oceanic age at the trench and low strain rate conditions a higher plate coupling and the inversion of the basin.

### 7.4. Nature and Origin of ENE and WSW Deep Structures

[38] Another pervasive tectonic feature of the western margin of South America is the widespread distribution of oblique-to-the-orogen crustal lineaments [e.g., *Katz*, 1971; *Yáñez et al.*, 1998], which cut the well-organized roughly N-S architecture of the Andean orogen. Such a disruptive array of structures can be well understood in a bulk compressive environment dominated by different shortening rates. In the proposed model, changes in the degree of coupling under constant convergence regime should be controlled by differences in age at the trench. Such a tectonic configuration is shown in the deformation model of Figure 8, in which the large coupling contrast generates an E-W flow pattern. Although this continuum approach cannot predict faulting patterns in the brittle domain, along-strike differences in shortening rate should be associated with E-W deformation zones as observed in different areas, and times, of the Andean convergence. Large age contrasts at the trench may be the result of the collision of fracture zones with a large age offset across them, like the Challenger and Mocha Fracture Zones in the Nazca Plate [see *Tebbens and Cande*, 1997]. In the present Nazca-South America plate configuration the Challenger Fracture Zone is almost coincident with the development of the Melipilla Fault zone [*Yáñez et al.*, 1998] and the northern end the southern Andes Central Depression (33°S).

On the other hand, the Mocha Fracture Zone is coincident with a dramatic reduction in the width of the Central Depression at 38°S [Lavenue and Cembrano, 1999]. In both cases the oceanic plate is younger northward to the fracture zone, and the model properly predicts a northward increment in the compressive regime under this configuration. Another disruptive element that may have driven E-W trending deformation zones is the collision of passive ridges such as the Juan Fernandez Ridge at 33°S [Yáñez *et al.*, 2002]. In this case, two competing mechanisms are present: (1) the rough topography of volcanic edifices that should tend to increase friction at the base of the overriding plate and (2) the thermal resetting and implied lowering of the slip layer viscosity that acts in the opposite sense. According to the dynamic trench topography analysis carried out in section 3 (Figure 5) the slip layer viscosity on passive ridge zones is lower than the surrounding zones, suggesting that the reduction in strength associated with the thermal effect is more important than the rough topography in the long-term at the larger scales considered by our model. This segment of the convergence is interesting because it is also associated with the flat slab zone (Figure 1), where plate coupling should be stronger, given the larger seismicity of the zone [e.g., Gutscher and Peacock, 2003]. However, such a large seismic activity is mostly concentrated within the cold oceanic plate rather than in the plate contact (M. Pardo, personal communication, 2003), as a direct result of the depressed asthenospheric wedge in the flat zone.

## 8. Conclusions

[39] 1. A conceptual model for the plate coupling and the associated continental deformation in the Andes is proposed. In this model, large-scale deformation of the forearc zone is mostly controlled by the absolute velocity of the oceanic plate, whereas the continental plate deformation is driven by convergence rates and age of the oceanic plate. Deformation of the arc and foreland region is ultimately the result of the ridge push force from the Atlantic and the resistance at the Benioff plane.

[40] 2. According to this model, plate coupling is mostly a function of the age at the trench and the convergence rate, through the following empirical relationship:  $\sigma_{\text{slip}} = 0.58V^{1/4} \text{ age}^{1.22}$  [MPa].

[41] 3. Plate coupling is expressed in terms of the slip layer parameter. Assuming a slip layer thickness of 10 km, the effective slip layer viscosity varies in the range of  $2\text{--}0.2 \times 10^{20}$  Pa s. Larger values are observed in the Arica elbow at 20°S, whereas minimum slip layer viscosity is obtained at the Taitao TJ at 46°S. Given the power law dependence of the slip layer viscosity, there is an inverse relationship with the convergent velocity.

[42] 4. For present-day convergence at the Andes the model predicts a coupling strength in the range of 30–90 MPa, in agreement with previous estimates of thrust faults in subducting environments.

[43] 5. The conceptual mechanism for the arc-foreland long-term deformation is applied to the last 28 Myr tectonic evolution of the southern Andes. The model predicts some relevant first-order features of the margin's morphology and tectonics, such as the present-day trench morphology; the observed shortening rate and the crustal thickness of the

Altiplano region; and the clockwise and counterclockwise rotations to the north and south of the Andean orocline.

[44] 6. The model also accounts for other first-order tectonic features of the Andean convergence, e.g., the segmentation of tectonic erosion, the development of the Central Depression, basin inversion during slow convergence, and the ubiquitous occurrence of ENE and WSW oblique-to-the orogen deformation zones in the central and southern Andes.

## Appendix A: The 1-D Dynamic Trench Topography Modeling

[45] Following Wdowinski's [1992] formulation, the long-term deformation along the Andean subduction zone can be seen as a 2-D deformable overriding plate in contact with a rigid subducting slab at the Wadatti-Benioff zone and the much weaker asthenospheric layer underneath (Figure A1). In this simple model the overriding plate is represented by a viscous rheology (constant), interacting through boundary conditions with the subducting slab and the asthenosphere. The subducting slab effect is represented by a convergence velocity transferred to the overriding viscous plate through a narrow region that accommodates most of the associated deformation as described by Shreve and Cloos [1986]. In this model the narrow region parallel to the Wadatti-Benioff zone is called the "slip layer," characterized by a much lower viscosity. The ratio between slip viscosity and slip thickness times the convergence velocity represents the degree of coupling of the subducting slab and overriding plate. At the base of the continental lithosphere the shear traction associated with the flow in the asthenosphere is neglected because its likely effect on the continental plate deformation affects primarily the back-arc region with a longer wavelength. The surface boundary condition has no effect unless it is located below the sea level; in this case it has a positive pressure effect scaled by the crust and water density contrast. The remaining boundary condition corresponds to the vertical side located far away in the foreland region of the overriding plate, as the velocity field is naturally imposed to zero.

[46] The governing equation that represents the physics of the problem involves the force balance equation, the continuity of incompressible materials, and a linear constitutive law for the viscous flow and is represented mathematically by the following normalized equation:

$$\eta \nabla^2 u - \nabla p = \rho \hat{\alpha} Gr,$$

where  $\eta$  is viscosity,  $u$  is velocity,  $p$  is pressure,  $\rho$  is density,  $\hat{\alpha} = (0\hat{x}, 1\hat{y})$ ,  $Gr$  is Grashof number,  $(g\rho_o x_o^2/\eta_o u_o)$ , and  $g$  is gravitational acceleration. In this equation, the nondimensional Grashof number represents the ratio between the buoyant and viscous (or tectonic) forces,  $\rho_o$ ,  $x_o$ ,  $\eta_o$ ,  $u_o$ , are the characteristic density ( $3300 \text{ kg/m}^3$ ), length (100 km), viscosity ( $1\text{--}5 \times 10^{22} \text{ Pa s}$ ), and plate velocity ( $5\text{--}10 \text{ cm/yr}$ ), respectively. The problem is solved using the PDE2D6.0 package for finite element partial differential equations, using sparse lineal system solvers, with 3000 triangular elements, and cubic element types. The problem is solved using the penalty formulation that replaces the pressure term for an incompressible fluid [e.g., Zienkiewicz and Taylor, 1991]. Simple Newtonian rheology is used in order to keep the



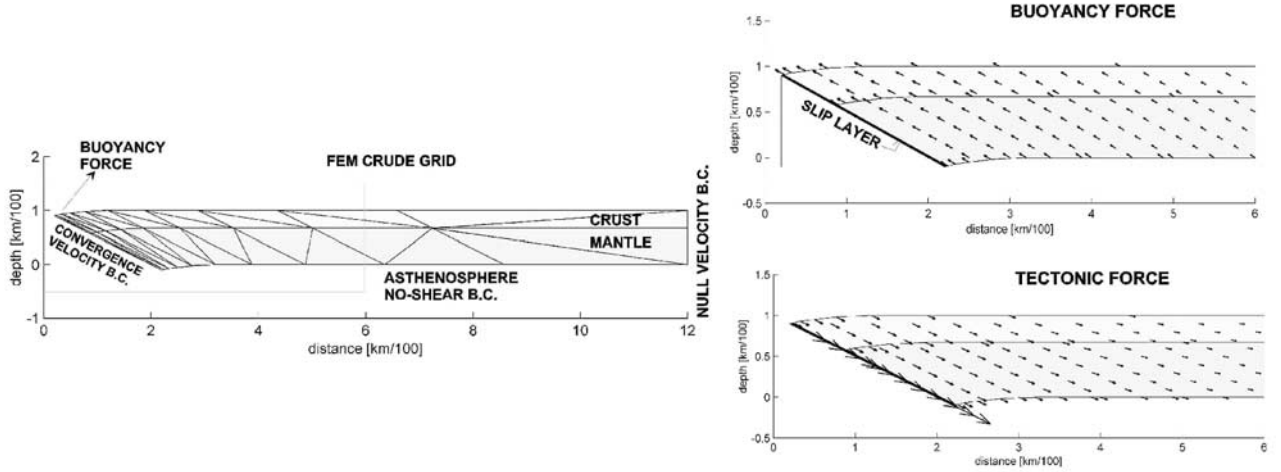


**Figure A1.** Viscous model deformation of the trench topography. (left) Mesh grid and boundary conditions. (right) Competing effects in the dynamic trench equilibrium. (top) Upward velocity flow associated with buoyancy forces of the less dense water column at the trench and continental slope. (bottom) Downward velocity flow associated with tectonic forces linked to the subducting oceanic lithosphere. Velocity fields represented with arrows are just referential, without any quantitative meaning.

model as simple as possible, but without losing the essentials of the mechanical problem (discussed in sections 2 and 4).

[47] The competing effects of the buoyant and tectonic forces in the near-trench topography deformation can clearly be observed in Figure A1. The associated velocity field, which ultimately controls the trench topography deformation, is spread in the opposite direction: Tectonic forces transfer the convergence velocity field downward and parallel to the Wadatti-Benioff plane, whereas buoyant forces try to reestablish the zero relief condition.

## Appendix B: Thermal Field at the Trench Zone

[48] In order to set some basic constraints on the thermal field ( $T$ ) developed in the slip layer zone, we solve the equation for conservation of heat in 2-D:

$$\frac{\partial T}{\partial t} + \mathbf{v} \cdot \nabla^2 T = \kappa \nabla^2 T + Q,$$

where  $\mathbf{v}$  is the velocity associated with the plate interaction and asthenospheric flow [e.g., *Turcotte and Schubert, 2002*],  $\kappa$  is the thermal diffusivity, and  $Q$  is a heat source term including all types of heat/sink sources (frictional, radiogenic, latent, etc.). Following *Davies and Stevenson [1992]* and *Daniel et al. [2001]* suggestions, we ignored the heat source contribution at the slip zone because it includes terms that tend to counterbalance each other (frictional heating + hydration versus melting + dehydration). Furthermore, heat sources are, at best, 1 order of magnitude smaller than the main controlling factor: The sink source associated with the advection of cold oceanic lithosphere [Davies and Stevenson, 1992]. We only considered the heat source in the continental lithosphere where radioactive sources decay exponentially with depth [e.g., *Turcotte and Schubert, 2002*]. In this simple experiment our main concern was the temperature field derived from the age-dependent advection term associated with the age of the subducting plate; therefore the velocity

field adopted is prescribed and independent of time. We used the total convergence velocity for the oceanic plate, the zero velocity for the overriding continental plate, and the associated corner flow analytical solution of *McKenzie [1967]* for the asthenosphere (see details in Figure A2). Thermal diffusivity was kept constant as  $\kappa = 1 \text{ mm/s}^{-2}$ , the mean value of olivine [e.g., *Holt, 1975*]. The thermal boundary conditions for the problem are described in Figure A2. We used the *Davies and Stevenson [1992]* boundary conditions that include zero temperature and heat flux on top and bottom surfaces, respectively. For the vertical sides the imposed conditions are the geothermal plate model for the oceanic plate, a linear geothermal for the continental side, and an adiabatic gradient for the asthenosphere. The age-dependent condition is controlled by the geothermal oceanic plate model [e.g., *Turcotte and Schubert, 2002*].

[49] The key role played by convergence velocity in the thermal state of the subduction region is well recognized [e.g., *Stern, 2002*]. Particularly relevant is its influence on the thermal state of the subducting slab and wedge zone [e.g., *McKenzie, 1967; Davies and Stevenson, 1992*]. In this thermal model we considered the range of convergent velocities for the Andean convergence (Table 1).

[50] Thermal model results are shown in Figure A3, considering end-member situations, old (50 Ma) and young (10 Ma) oceanic plate age at the trench, and slow (3 cm/yr) and fast (9 cm/yr) convergent velocity. The numerical problem was solved using Femlab code with 1600 Lagrange quadratic elements. The models were run for a period of 10 Myr until a steady condition was reached. The shape of the forearc geothermal field is controlled by the advection of the cold oceanic lithosphere, and therefore geothermal lines are subparallel to the slip zone.

## Appendix C: Strength of the Slip Layer Zone

[51] Following *Brace and Kohlstedt [1980]*, the differential stress state at fracturing is taken to be  $\Delta\sigma_b = Bgz$ ,

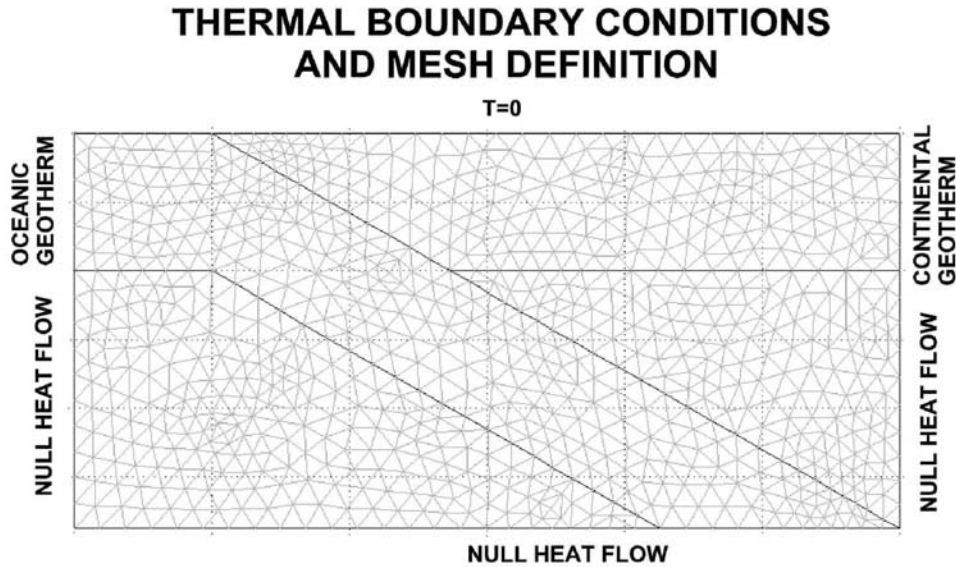


**Figure A2.** Mesh domain for the thermal computation of the forearc arc temperature field. Velocity field for the advection term in the energy equation is prescribed from corner-flow analytical models [McKenzie, 1967]. Thermal boundary conditions also are shown.

where  $B$  is a constant that depends on the pore fluid pressure and fault nature (0.5–0.8 in subduction thrust faults [Gerya *et al.*, 2002]) and  $g$  and  $z$  are the acceleration gravity and depth, respectively. Creep deformation at high temperatures follows a power law [e.g., Evans and Kohlstedt, 1995]:  $\Delta\sigma_d = (\dot{\epsilon}/A)^{1/n} \exp(E/nRT)$ , where  $\dot{\epsilon}$ ,  $A$ ,  $n$ ,  $E$ ,  $R$ ,  $T$

are the strain rate [ $\text{s}^{-1}$ ], material constant [ $\text{Pa}^{-n} \text{s}^{-1}$ ], stress exponent, activation energy [ $\text{kJ mol}^{-1}$ ], gas constant ( $8.31 \text{ J mol}^{-1} \text{ } ^\circ\text{K}^{-1}$ ), and absolute temperature [ $^\circ\text{K}$ ], respectively. The appropriate rheology for the slip layer zone is certainly not well constrained, and a thorough analysis of this issue is beyond the scope of this commu-

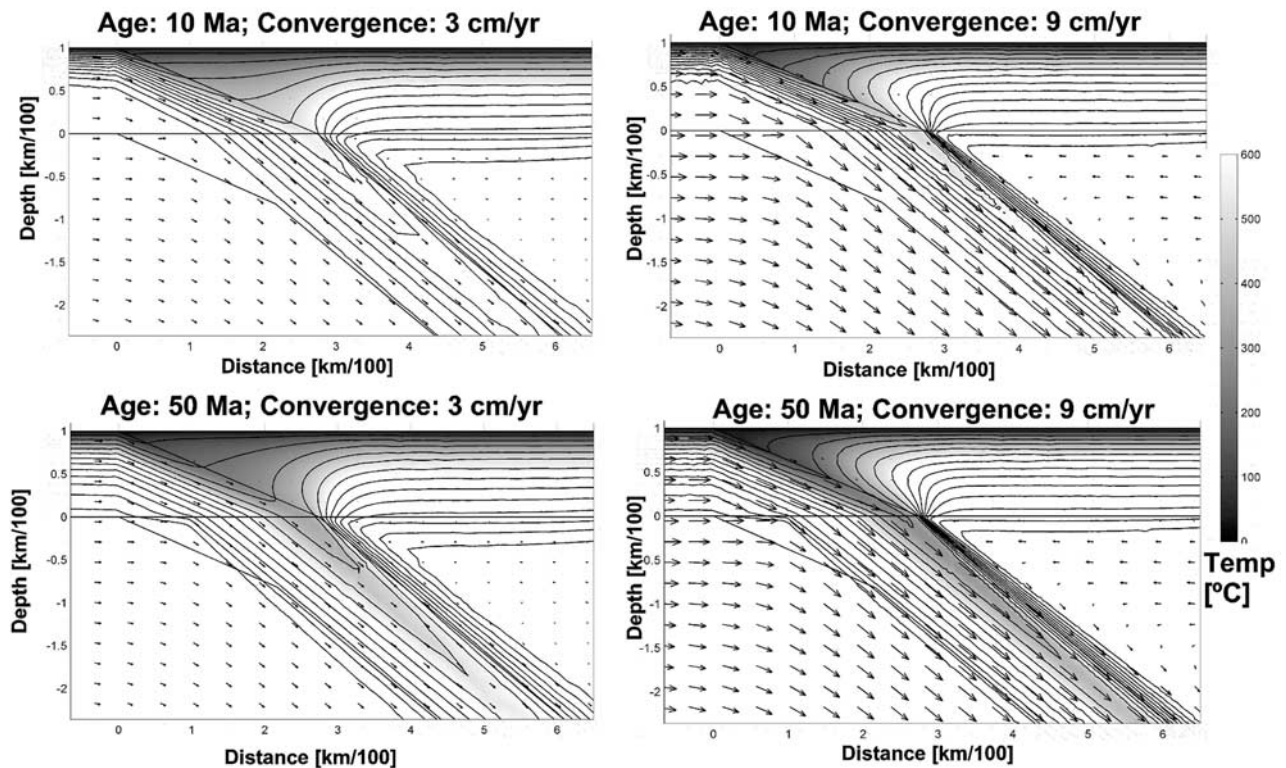


**Figure A3.** End-member temperature dependence of the slip layer zone. Contour lines are spaced every  $100^\circ\text{C}$ . Prescribed velocity field for the subduction zone is shown in black arrows. (top) A subducting lithosphere of 10 Ma at the trench, for (left) 3 and (right) 9 cm/yr, respectively. (bottom) A subducting lithosphere of 50 Ma at the trench for (left) 3 and (right) 9 cm/yr, respectively.



nification. Following Gerya *et al.*'s [2002] discussion, we adopt a wet olivine rheology for the mantle ( $A = 10^{3.3} \text{ Pa}^{-n} \text{ s}^{-1}$ ,  $n = 4$ ,  $E = 470 \text{ kJ mol}^{-1}$ ) and a quartz diorite rheology for the crust ( $A = 2 \times 10^4 \text{ Pa}^{-n} \text{ s}^{-1}$ ,  $n = 2.4$ ,  $E = 219 \text{ kJ mol}^{-1}$ ). Constant  $B$  for the brittle behavior is fixed in 0.5. The strain rate at the slip zone is the ratio of the convergence velocity and the slip layer thickness (fixed arbitrarily to 10 km).

[52] **Acknowledgments.** This paper was supported by Fondecyt grant 1000136. We wish to thank the thorough and useful reviews by journal referees Giorgio Spada, Claudio Faccenna, and an anonymous reviewer that helped to improve the quality, clarity, and scope of this manuscript. Our view of the Andean processes has been greatly influenced by and benefited from stimulating discussions with Myrl Beck, Constantino Mpodozis, Mario Pardo, Victor Ramos, and Andres Tassara.

## References

- Aberg, G., L. Aguirre, B. Levi, and J. Nystrom (1984), Spreading subsidence and generation of ensialic marginal basins: An example from the Early Cretaceous of central Chile, in *Marginal Basin Geology: Volcanic and Associated Sedimentary and Tectonic Processes in Modern and Ancient Marginal Basins*, edited by B. P. Kokelaar and M. F. Howells, *Geol. Soc. Spec. Publ.*, 16, 185–193.
- Allmendinger, R. W., D. Figueroa, D. Snyder, J. Beer, C. Mpodozis, and B. L. Isacks (1990), Foreland shortening and crustal balancing in the Andes at 30°S latitude, *Tectonics*, 9, 789–809.
- Arriagada, C., P. Roperch, and C. Mpodozis (2000), Clockwise block rotations along the eastern border of the Cordillera de Domeyko, northern Chile (22°45′–23°30′S), *Tectonophysics*, 326, 153–171.
- Arriagada, C., P. Roperch, C. Mpodozis, G. Dupont-Nivet, P. R. Cobbold, A. Chauvin, and J. Cortés (2003), Paleogene clockwise tectonic rotations in the forearc of central Andes, Antofagasta region, northern Chile, *J. Geophys. Res.*, 108(B1), 2032, doi:10.1029/2001JB001598.
- Baby, P., P. Rochat, G. Mascle, and G. Hérail (1997), Neogene shortening contribution to crustal thickening in the back arc of the central Andes, *Geology*, 25, 883–886.
- Beck, M. E., R. F. Burmester, R. E. Drake, and P. D. Riley (1994), A tale of two continents: Some tectonic contrasts between the central Andes and the North American Cordillera, as illustrated by their paleomagnetic signatures, *Tectonics*, 13, 215–224.
- Bird, P. (1988), Formation of the Rocky Mountains, western United States: A continuum computer model, *Science*, 239, 1501–1507.
- Bird, P., and K. Piper (1980), Plane-stress finite element models of tectonic flow in southern California, *Phys. Earth Planet. Inter.*, 21, 158–175.
- Brace, W. F., and D. L. Kohlstedt (1980), Limits on lithospheric stress imposed by laboratory experiments, *J. Geophys. Res.*, 85, 6248–6252.
- Cembrano, J., E. Schermer, A. Sanhueza, and A. Lavenue (2000), Along strike-variations in the nature and timing of deformation along an intra-arc shear zone, the Liqueñe Ofqui fault zone, southern Chilean Andes, *Tectonophysics*, 319, 129–149.
- Christensen, U. R. (1992), A Eulerian technique for thermomechanical modeling of lithospheric extension, *J. Geophys. Res.*, 97, 2015–2036.
- Daniel, A., N. J. Kusznir, and P. Styles (2001), Thermal and dynamic modeling of deep subduction of a spreadin center: Implications for the fate of the subducted Chile Rise, southern Chile, *J. Geophys. Res.*, 106, 4293–4304.
- David, C., D. Comte, J. Martinod, L. Dorbath, G. Hérail, C. Dorbath, and H. Haessler (2002), Intracontinental seismicity and neogene deformation of the Andean forearc in the region of Arica, (18.5°S–19.5°S), paper presented at Fifth International Symposium on Andean Geodynamics, Dep. de Geofis., Univ. de Chile, Toulouse, France.
- Davies, J. H., and D. J. Stevenson (1992), Physical models of source region of subduction zone volcanics, *J. Geophys. Res.*, 97, 2037–2070.
- DeMets, C., et al. (1994), Effects of recent revisions to the geomagnetic reversal time scale on estimates of current plate motions, *Geophys. Res. Lett.*, 21, 2191–2194.
- Dewey, J. F., and P. Bird (1970), Mountain Belt and the new global tectonics, *J. Geophys. Res.*, 75, 2625–2647.
- Dewey, J. F., and S. H. Lamb (1992), Active tectonics of the Andes, *Tectonophysics*, 205, 79–95.
- England, P. (1983), Constraints on extension of continental lithosphere, *J. Geophys. Res.*, 88, 1145–1152.
- England, P. C., and D. P. McKenzie (1982), A thin viscous sheet model for continental deformation, *Geophys. J. R. Astron. Soc.*, 70, 295–321. (Correction to: A thin viscous sheet model for continental deformation, *Geophys. J. R. Astron. Soc.*, 73, 523–532, 1983.)
- Evans, B., and D. L. Kohlstedt (1995) Rheology of rocks, in *Rock physics and phase relations, A handbook of physical constants*, AGU Ref. Shelf, vol. 3, edited by T. J. Ahrens, pp. 148–165, AGU, Washington, D. C.
- Froidevaux, C., and B. L. Isacks (1984), The mechanical state of the lithosphere in the Altiplano-Puna segment of the Andes, *Earth Planet. Sci. Lett.*, 71, 305–314.
- Gerya, T., B. Stöckhert, and A. L. Perhuck (2002), Exhumation of high-pressure metamorphic rocks in a subduction channel: A numerical simulation, *Tectonics*, 21, 1–15.
- González, G., J. Cembrano, D. Carrizo, A. Macci, and H. Schneider (2003), The link between forearc tectonics and Pliocene-Quaternary deformation of the Coastal Cordillera, northern Chile, *J. S. Am. Earth Sci.*, 16, 321–342.
- Gordon, R. G., and D. M. Jurdy (1986), Cenozoic global plate motions, *J. Geophys. Res.*, 91, 12,389–12,406.
- Gregory-Wodzicki, K. M. (2000), Uplift history of the central and northern Andes: A review, *Geol. Soc. Am. Bull.*, 112, 1091–1105.
- Gutscher, M. A. (2002), Andean subduction styles and their effect on thermal structure and interplate coupling, *J. S. Am. Earth Sci.*, 15, 3–10.
- Gutscher, M.-A., and S. M. Peacock (2003), Thermal models of flat subduction and the rupture zone of great subduction earthquakes, *J. Geophys. Res.*, 108(B1), 2009, doi:10.1029/2001JB000787.
- Gutscher, M. A., W. Spakman, H. Bijwaard, and E. R. Engdahl (1999), Geodynamics of flat slab subduction: Seismicity and tomographic constraints from the Andean margin, impact of the Carnegie Ridge collision, *Earth Planet. Sci. Lett.*, 168, 255–270.
- Gutscher, M. A., J. Malavieille, S. Lallemand, and J. Y. Collot (2000), Tectonic segmentation of the North Andean Margin: Impact, *Tectonics*, 19, 814–833.
- Hindle, D., J. Kley, E. Klosko, S. Stein, T. Dixon, and E. Norambuena (2002), Consistency of geological and geodetic displacements during Andean orogenesis, *Geophys. Res. Lett.*, 29, 1–4.
- Holt, J. B. (1975), Thermal diffusivity of olivine, *Earth Planet. Sci. Lett.*, 27, 404–408.
- Isacks, B. L. (1988), Uplift of the Central Andes Plateau, and the bending of the Bolivian orocline, *J. Geophys. Res.*, 93, 3211–3231.
- Jarrard, R. D. (1986), Relations among subduction parameters, *Rev. Geophys.*, 24, 217–284.
- Jischke, M. D. (1975), On the dynamics of descending lithosphere plates and slip zones, *J. Geophys. Res.*, 80, 4809–4813.
- Jordan, T. E., and R. W. Allmendinger (1986), The Sierras Pampeanas of Argentina: A modern analogue of the Laramide deformation, *Am. J. Sci.*, 286, 737–764.
- Jordan, T. E., B. L. Isacks, V. Ramos, and R. W. Allmendinger (1983), Mountain building in the central Andes, *Episodes*, 3, 20–25.
- Jordan, T., W. Burns, R. Veiga, F. Pángaro, P. Copeland, S. Kelley, and C. Mpodozi (2001), Extension and basin formation in the Southern Andes caused by increased convergence rate: A Mid-Cenozoic trigger for the Andes, *Tectonics*, 20, 308–324.
- Katz, H. R. (1971), Continental margin in Chile: Is tectonic style compressional or extensional?, *Am. Assoc. Pet. Geol. Bull.*, 55, 1753–1758.
- Lamb, S., and L. Hoke (1997), Origin of the high plateau in the central Andes, Bolivia, South America, *Tectonics*, 16, 623–649.
- Lavenue, A., and J. Cembrano (1999), Compressional and transpressional stress pattern for the Pliocene and Quaternary (Andes of central and southern Chile), *J. Struct. Geol.*, 21, 1669–1691.
- McKenzie, D. P. (1967), Speculations on the consequences and causes of plate motions, *Geophys. J. R. Astron. Soc.*, 18, 1–32.
- McQuarrie, N. (2002a), The kinematic history of the central Andean fold-thrust belt, Bolivia: Implications for building a high plateau, *Geol. Soc. Am. Bull.*, 114, 950–963.
- McQuarrie, N. (2002b), Initial plate geometry, shortening variations and evolution of the Bolivian Orocline, *Geology*, 30, 867–870.
- Molnar, P., and P. England (1990), Temperatures, heat flux, and frictional stress near major thrust faults, *J. Geophys. Res.*, 95, 4833–4856.
- Mpodozis, C., and V. Ramos (1990), The Andes of Chile and Argentina, in *Geology of the Andes and Its Relation to Hydrocarbon and Mineral Resources*, *Earth Sci. Ser.*, vol. 11, edited by G. E. Erickson et al., pp. 59–90, Circum-Pac. Council for Energy and Miner. Resour., Houston, Tex.
- Muller, J. P., J. Kley, and V. Jacobshagen (2002), Structure and Cenozoic kinematics of the eastern Cordillera, *Tectonics*, 21, 1–24.
- Muñoz, N., and R. Charrier (1996), Uplift of the western border of the Altiplano on a west-vergent thrust system, northern Chile, *J. S. Am. Earth Sci.*, 9, 171–181.
- Parada, M. A., B. Levi, and J. O. Nystrom (1991), Geochemistry of the Triassic to Jurassic plutonism of central Chile (30–33°S); petrogenetic implications and tectonic discussion, in *Andean Magmatism and Its Tectonic Setting*, edited by R. S. Harmon and C. W. Rapela, *Spec. Pap. Geol. Soc. Am.*, 265, 99–112.



- Pardo, M., T. Monfret, E. Vera, A. Eisenberg, G. Yáñez, and E. Triep (2003), Cambio en la subducción de la placa de Nazca, de plana a inclinada, bajo Chile central y Argentina: Datos sismológicos preliminares, paper presented at 10th Congreso Geológico Chileno, Concepción, Chile.
- Ramos, V. A. (1985), El Mesozoico de la alta cordillera de Mendoza: Reconstrucción tectónica de sus facies- Argentina, in *Actas IV Chile Congreso Geológico Chileno*, vol. 2, 104–118, Univ. del Norte, Antofagasta, Chile.
- Ramos, V. A. (1988), The tectonics of the central Andes; 30° to 33°S latitude, in *Processes in Continental Lithospheric Deformation*, edited by S. Clark and D. Burchfiel, *Spec. Pap. Geol. Soc. Am.*, 218, 31–54.
- Ramos, V. A. (1989), Foothills structure in northern Magallanes Basin, Argentina, *AAPG Bull.*, 73, 887–903.
- Ranalli, G. (1995), *Rheology of the Earth*, 2nd ed., 413 pp., Chapman and Hall, New York.
- Roperch, P., M. Fornari, G. Hérail, and G. Parraguez (2000), Tectonic rotations within the Bolivian Altiplano: Implications for the geodynamic evolution of the central Andes during the late Tertiary, *J. Geophys. Res.*, 105, 795–820.
- Rubio, E., M. Torne, E. Vera, and A. Díaz (2000), Crustal structure of the southernmost Chilean margin from seismic and gravity data, *Tectonophysics*, 323, 39–60.
- Scholz, C. H., and J. Campos (1995), On the mechanism of seismic decoupling and back-arc spreading at subduction zones, *J. Geophys. Res.*, 100, 22,103–22,115.
- Schult, F. R., and R. G. Gordon (1984), Root-mean-square velocities of the continents with respect to the hot spots since the early Jurassic, *J. Geophys. Res.*, 91, 10,229–10,245.
- Shreve, R. L., and M. Cloos (1986), Dynamics of sediment subduction, melange formation, and prism accretion, *J. Geophys. Res.*, 91, 10,229–10,245.
- Smith, W. H. F., and D. T. Sandwell (1994), Bathymetric prediction from dense satellite altimetry and sparse shipboard bathymetry, *J. Geophys. Res.*, 99, 21,803–21,824.
- Somoza, R. (1998), Updated Nazca (Farallon)-South America relative motions during the last 40 Ma: Implication for mountain building in the central Andean region, *J. S. Am. Earth Sci.*, 11, 211–215.
- Stern, C. (1991), Role of subduction erosion in the generation of Andean magmas, *Geology*, 19, 78–81.
- Stern, R. J. (2002), Subduction zones, *Rev. Geophys.*, 40, 1–37.
- Tebbens, S. F., and S. C. Cande (1997), Southeast Pacific tectonic evolution from early Oligocene to Present, *J. Geophys. Res.*, 102, 12,061–12,084.
- Turcotte, D. L., and G. Schubert (2002), *Geodynamics: Applications of Continuum Physics to Geological Problems*, 450 pp., John Wiley, Hoboken, N. J.
- Uyeda, S., and H. Kanomari (1979), Back-arc opening and the mode of subduction, *J. Geophys. Res.*, 84, 1049–1061.
- von Huene, R., and C. R. Ranero (2003), Subduction erosion and basal friction along the sediment-starved convergent margin off Antofagasta, Chile, *J. Geophys. Res.*, 108(B2), 2079, doi:10.1029/2001JB001569.
- Wdowinski, S. (1992), Dynamically supported trench topography, *J. Geophys. Res.*, 97, 17,651–17,656.
- Wdowinski, S., and Y. Bock (1994), The evolution of deformation and topography of high elevated plateaus: 1. Model, numerical analysis, and general results, *J. Geophys. Res.*, 99, 7103–7119.
- Wdowinski, S., and R. J. O'Connell (1990), On the choice of boundary conditions in continuum models of continental deformation, *Geophys. Res. Lett.*, 17, 2413–2416.
- Yáñez, G., P. Gana, and R. Fernández (1998), Origen y significado geológico de la Anomalia Melipilla, Chile central, *Rev. Geol. Chile*, 25, 175–198.
- Yáñez, G., C. R. Ranero, R. von Huene, and J. Díaz (2001), Magnetic anomaly interpretation across the southern central Andes (32°–34°): The role of the Juan Fernández Ridge in the late Tertiary evolution of the margin, *J. Geophys. Res.*, 106, 6325–6345.
- Yáñez, G., J. Cembrano, M. Pardo, C. Ranero, and D. Selles (2002), The Challenger-Juan Fernandez-Maipo major tectonic transition of the Nazca-Andean subduction system at 33–34°S: Geodynamic evidence and implications, *J. S. Am. Earth Sci.*, 15, 23–38.
- Zienkiewicz, O. C., and R. L. Taylor (1991), *The Finite Element Method*, vol. 2, *Solid and Fluid Mechanics Dynamics and Non-linearity*, 4th ed., McGraw-Hill, New York.

J. Cembrano, Departamento de Ciencias Geológicas, Universidad Católica del Norte, Avda. Angamos 0610, Antofagasta, Chile. (jcembrano@ucn.cl)

G. Yáñez, CODELCO-CHILE, Teatinos 258 7° Piso, Santiago, Chile. (gyane003@stgo.codelco.cl)